Technische Universität Dresden
Bereich Mathematik und Naturwissenschaften
Fakultät Physik
Helmholtz-Zentrum Dresden-Rossendorf
Institut für Strahlenphysik
Laser-Teilchenbeschleunigung

Masterarbeit
zur Erlangung des Hochschulgrades
Master of Science
im Studiengang
Physik

Implementation and validation of a method for using experimentally measured laser profiles in laser-plasma simulations with PIConGPU

vorgelegt von
Fabia Dietrich
geboren am 22.02.2000 in Hartmannsdorf

eingereicht am 16.01.2025

Erstgutachter: Prof. Dr. Ulrich Schramm
Zweitgutachter: Prof. Dr. Thomas Cowan

Abstract

In laser-plasma physics, particle-in-cell (PIC) simulations are an indispensable tool for investigating laser-matter interactions. However, traditional simulations often rely on idealized laser profiles, neglecting the complexities of real-world laser pulses. This thesis addresses this weakness by developing a novel laser profile for PIConGPU, a PIC simulation software, that enables incorporating laboratory-measured laser field data into simulations. By leveraging these realistic inputs, the implementation enables the creation of a digital twin of experimental setups, providing a platform to explore, recreate and predict experimental outcomes. Crucially, this approach facilitates the study of spatio-temporal couplings in ultra-short laser pulses, which mostly cannot be described analytically, and offers new insights into their influence on laser-driven particle acceleration. This work enables bridging the gap between simulation and experiment, which will enhance our understanding of laser-plasma dynamics and pave the way for more precise experimental designs.

Zusammenfassung

Particle-In-Cell-Simulationen (PIC) sind ein unverzichtbares Instrument zur Untersuchung von Laser-Materie-Wechselwirkungen in der Laser-Plasma-Physik. Herkömmliche Simulationen basieren jedoch oft auf idealisierten Laserprofilen und vernachlässigen die Komplexität realer Laserpulse. Diese Arbeit adressiert diesen Umstand mit der Entwicklung eines neuen Laserprofils für PIConGPU, eine PIC-Simulationssoftware, das es ermöglicht, im Labor gemessene Laserfelddaten in Simulationen einzubeziehen. Durch die Nutzung eines realistischen Laser-Profils ermöglicht die Implementierung die Erstellung eines “digital twins” von Versuchsaufbauten und bietet damit eine Plattform zur Untersuchung, Nachbildung und Vorhersage von Versuchsergebnissen. Entscheidend ist, dass dieser Ansatz die Untersuchung von Laser-Dispersionen erleichtert, die in vielen Fällen nicht analytisch beschrieben werden können, und neue Einblicke in ihren Einfluss auf die lasergetriebene Teilchenbeschleunigung bietet. Diese Arbeit ermöglicht es, die Lücke zwischen Simulation und Experiment zu schließen, was unser Verständnis der Laser-Plasma-Dynamik verbessern und den Weg für präzisere experimentelle Designs ebnen wird.

Contents

List of Figures

List of Tables

1 Introduction

Laser-plasma physics is an important field of modern research with wide-ranging applications in areas such as particle acceleration for medical purposes [1] or inertial confinement fusion [2], and high-energy-density physics [3]. A fundamental challenge in this field is understanding and controlling the complex interaction between high-intensity laser pulses and plasma, processes that are difficult to fully unravel and analyze through experiments alone [4, 5]. Simulations have become indispensable tools for bridging this gap, enabling us to reproduce experimental conditions [6], test hypotheses [7], and gain deeper insights into the underlying physical processes [8, 9].

A central tool in modelling laser-plasma interactions are Particle-in-Cell (PIC) simulations [10], which calculate the dynamics of a plasma based on Maxwell's equations in a discretized simulation volume. However, the accuracy of such simulations depends on realistic input parameters that closely mimic experimental conditions. A significant limitation in many simulation codes is the assumption of idealized laser conditions, such as perfectly Gaussian beams [11]. In reality, experimental laser fields deviate from the perfect Gaussian shape due to inevitable intrinsic spatio-temporal couplings (STCs). Most likely, STCs are introduced in the laser pulse even on purpose, as many applications depend on them - for example chirped pulse amplification [12], which recently has been awarded with a Nobel prize. Recent experiments at HZDR show, that laser dispersion also influences the properties of accelerated particles profoundly [13]. For instance, the laser-wakefield accelerator (LWFA) performance can be optimized by tweaking the spectral phase of the driver laser, which affects the final electron beam parameters significantly (see figure 1.1) [14].

The scope of this master thesis is to address the lack of realistic laser simulations by implementing a respective laser profile in PIConGPU, a multi-GPU PIC simulation code being developed at HZDR. Together with a measurement of the utilized gas profile, this allows to create a digital twin of experimental setups, which is essential for understanding how specific laser parameters, and especially STCs, influence particle acceleration. Such knowledge can opens up pathways to predictions onto optimized experimental designs.

A promising starting condition for realistic simulations is provided by INSIGHT measurements, which provide the full field information of a laser pulse at the focus position. Measurement results from the DRACO Ti:Sapphire chirped pulse amplification laser system at HZDR are already available and allow a complete characterization of the field at its focal spot. However, such an INSIGHT measurement demands certain processing steps before serving as simulation input. Those steps

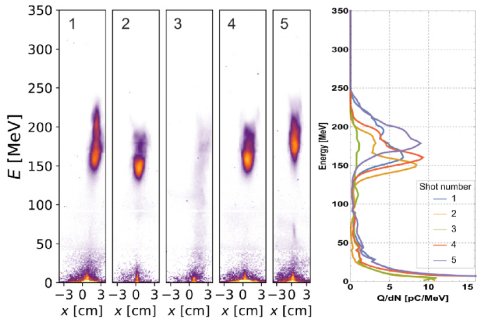

(a) GVD=-100 fs^2,τ=28±2 fs

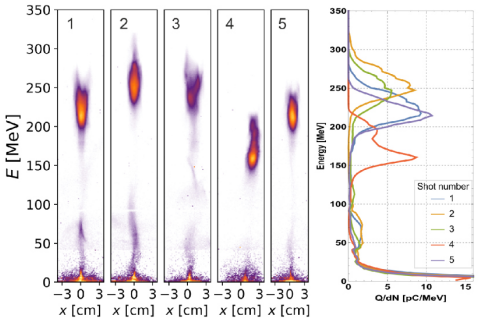

(b) GVD=0 fs^2,τ=27±2 fs

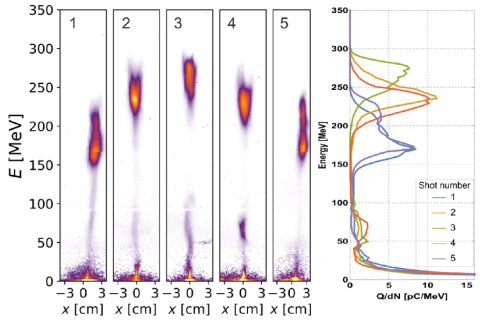

(c) GVD=+100 fs^2,τ=31±2 fs

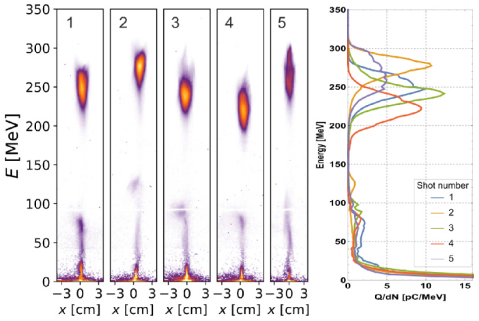

(d) GVD=+200 fs^2,τ=40±4 fs

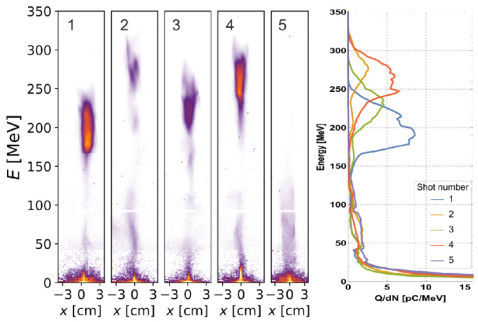

(e) GVD=+300 fs^2,τ=43±4 fs

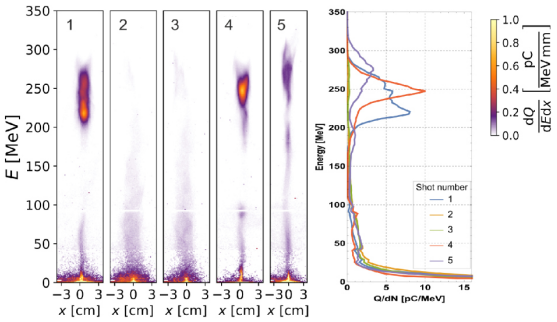

(f) GVD=+400 fs^2,τ=48±5 fs

Figure 1.1: Influence of group velocity dispersion (GVD) on the LWFA performance. Shown are the electron spectrometers of consecutive shots with the DRACO Ti:Sapphire chirped pulse amplification laser system at HZDR. ©2018 Dr. Arie Irman

are presented in detail in chapter 3 and have been implemented in a python script, which now forms part of the PIConGPU repository.

The subsequent procedure of reading such a realistic laser pulse into a PIConGPU simulation is explained in chapter 4, and the newly developed respective laser profile became part of the PIConGPU repository, too.

In the end, first LWFA simulations using the novel realistic laser profile will be presented and analyzed, and an outlook onto its widespread application possibilities will be given.

2 Theory

2.1 Diffraction theory

Diffraction theory is essential in describing and predicting how electromagnetic fields propagate and transform when being focused. In this chapter, the foundational formulas and mathematical tools used in diffraction theory will be introduced, including the Huygens-Fresnel principle and Fourier optics. These will subsequently be used to propagate experimentally measured laser fields through space, and to draw the connection between near-, mid-, and far-field.

The last part of this chapter introduces the Gaussian beam and some of the most important dispersion parameters as a tool to describe experimentally measured laser fields mathematically.

2.1.1 The Helmholtz equation

The Helmholtz equation is a scalar wave equation for the electric field. It can be derived from Maxwell's equations, which are the most fundamental part of classical electromagnetism and can be written as

$$\nabla \cdot \boldsymbol{E} = \frac{\rho}{\varepsilon_0} \tag{2.1}$$

$$\nabla \cdot \boldsymbol{B} = 0 \tag{2.2}$$

$$\nabla \times \boldsymbol{E} = -\frac{\partial \boldsymbol{B}}{\partial t} \tag{2.3}$$

$$\nabla \times \boldsymbol{B} = \mu_0 \left(\boldsymbol{J} + \varepsilon_0 \frac{\partial \boldsymbol{E}}{\partial t} \right) \tag{2.4}$$

where $\boldsymbol{E}$ denotes the electric field, $\boldsymbol{B}$ the magnetic field, ε_0 the vacuum permittivity and μ_0 the vacuum permeability. By applying the $\nabla\times$ operation to (2.3), utilizing the vector identity

$$\nabla \times (\nabla \times \boldsymbol{E}) = \nabla(\nabla \cdot \boldsymbol{E}) - \nabla^2 \mathbf{E}$$

and assuming the absence of electric current $\boldsymbol{J} = 0$, one obtains the wave equation for the electric field

$$\nabla^2 \boldsymbol{E} - \frac{1}{c^2} \frac{\partial^2 \boldsymbol{E}}{\partial t^2} = 0, \tag{2.5}$$

where $c = 1/\sqrt{\mu_0 \varepsilon_0}$ denotes the speed of light.

The time derivative in the second term of (2.5) can be solved by transforming the electric field into the spectral domain with a one-dimensional Fourier transform

$$\tilde{\boldsymbol{E}}(\boldsymbol{r},\omega) = \int \boldsymbol{E}(\boldsymbol{r},t)\; e^{-i\omega t} dt. \tag{2.6}$$

The inverse Fourier transform is defined as

$$\boldsymbol{E}(\boldsymbol{r},t) = \frac{1}{2\pi} \int \tilde{\boldsymbol{E}}(\boldsymbol{r},\omega)\; e^{i\omega t} d\omega \tag{2.7}$$

Inserting (2.7) into (2.5) subsequently leads to the *Helmholtz equation*

$$\left[\nabla^2 + \left(\frac{\omega}{c}\right)^2\right] \tilde{\boldsymbol{E}} = 0, \tag{2.8}$$

which decouples the electric field components, so that the vector field $\tilde{\boldsymbol{E}}$ can be treated as a scalar field $\tilde{\boldsymbol{E}} = \tilde{E}\, \boldsymbol{e}_p$, described by a polarisation vector $\boldsymbol{e}_p$. Substituting for the wave number k, which is defined as $k = \omega/c$[1], finally results in

$$\left(\nabla^2 + k^2\right) \tilde{E} = 0. \tag{2.9}$$

2.1.2 Angular spectrum propagation

An easy solution of (2.9) is a unit-amplitude plane wave, travelling into positive z direction

$$\tilde{E}(z) = e^{-ikz}$$

Hence, plane wave propagation from $z = 0$ to an arbitrary z mathematically corresponds to a multiplicative phase factor e^{-ikz}. This knowledge can be applied to propagate any unspecified monochromatic source, for example a laser, along the z direction, when its complex transverse field distribution is known in the plane $z = 0$.

Let $U_0(x, y, \omega) = U(x, y, z = 0, \omega)$ be this incident transverse field distribution. The goal is to calculate the propagated field $U(x, y, z, \omega)$ at a distance $z > 0$ (or the back-propagated field at $z < 0$). As a first step, the incident field is decomposed into plane waves with a two-dimensional inverse Fourier transform with respect to the two transverse spatial axes x and y,

$$\hat{\tilde{U}}_0(k_x, k_y, \omega) = \iint_{-\infty}^{\infty} \tilde{U}_0(x, y, \omega)\; e^{i(k_x x + k_y y)}\; dx\; dy, \tag{2.10}$$

which is also called the *angular spectrum* of U_0. Being in the spatial frequency domain, propagation out of $z = 0$ is described mathematically by a multiplication with the complex phase $e^{-ik_z z}$, where the wave vector k_z is described as

$$k_z = \sqrt{\left(\frac{\omega}{c}\right)^2 - k_x^2 - k_y^2}. \tag{2.11}$$

[1] This definition originates from the (inverse) spatial Fourier transform (2.10), which transforms the Helmholtz equation (2.8) to $(-\boldsymbol{k}^2 + (\omega/c)^2)\, \hat{\tilde{E}} = 0$

Please note, that for certain values of k_x and k_y, k_z can be imaginary. In this case, the factor would then be real instead of complex,

$$e^{-\sqrt{k_x^2+k_y^2-(\omega/c)^2}\ |z|},$$

which leads to evanescent instead of propagating waves. The absolute value of z assures the evanescent behaviour also for $z < 0$.

Now, all the propagated plane waves have to be "added up" by a two-dimensional Fourier transform back to the spatial domain to obtain the propagated field at $z \neq 0$

$$\tilde{U}(x,y,z,\omega) = \iint_{-\infty}^{\infty} \hat{\tilde{U}}_0(k_x,k_y,\omega)\ e^{-ik_z z}\ e^{-i(k_x x+k_y y)}\ dk_x\ dk_y \tag{2.12}$$

for real k_z and

$$\tilde{U}(x,y,z,\omega) = \iint_{-\infty}^{\infty} \hat{\tilde{U}}_0(k_x,k_y,\omega)\ e^{-\sqrt{k_x^2+k_y^2-(\frac{\omega}{c})^2}|z|}\ e^{-i(k_x x+k_y y)}\ dk_x\ dk_y$$

for imaginary k_z. The electric field E is connected to U by $E = \mathcal{R}e\{U\}$.

This solution is exact, and its numerical implementation is relatively simple, as it relies solely on Fourier transforms. However, its advantages are limited when applied to the numerical propagation of diverging fields, such as a laser beam moving out of the focal plane. To avoid Fourier transform artifacts, the transverse field distribution must approach zero (or at least close to zero) at the boundaries of the window. Consequently, the method's propagation distance is restricted by the growing spot size. It is possible to extend the window size by padding zeros around its borders, but this increases the computational effort, as the number of rows of padded zeros contributes quadratically to the calculation. Therefore, another method is needed to propagate a transverse (laser) field distribution from the focus position (= far field) to before the focusing element (= near field) and vice versa.

2.1.3 Fresnel Diffraction

The propagation of a given complex transverse field distribution can also be described using the *Rayleigh-Sommerfeld diffraction formula* [15]

$$U(P_0) = \frac{i}{\lambda} \iint_{\Sigma} U(P_1)\ \cos(\boldsymbol{n},\boldsymbol{r}_{01})\ \frac{e^{-ikr_{01}}}{r_{01}}\ dS, \tag{2.13}$$

which characterizes diffraction through a planar aperture Σ, as depicted in figure 2.1. P_0 lies in propagation direction behind the screen and P_1 within Σ, $\boldsymbol{r}_{01}$ connects those points, $\boldsymbol{n}$ is the normal vector on Σ and $\lambda = 2\pi/k$ is the wave length.

The "quasi-physical" interpretation of (2.13) suggests that the observed field $U(P_0)$ can be expressed as superposition of diverging spherical waves originating from secondary sources located at every point P_1 along Σ (*Huygen's principle*).

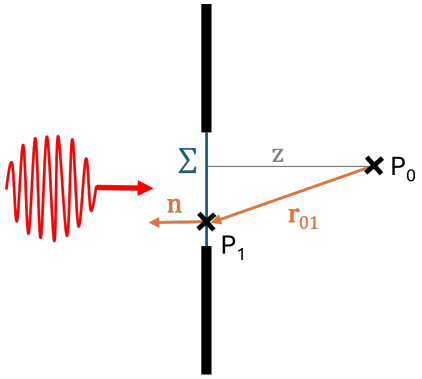

Figure 2.1: Diffraction by a planar screen (Rayleigh-Sommerfeld). An incident field (red) passes the aperture Σ from left to right.

Using $\cos(\boldsymbol{n}, \boldsymbol{r}_{01}) = z/r_{01}$, (2.13) can be rewritten as

$$U(x,y,z) = \frac{iz}{\lambda} \iint_{-\infty}^{\infty} U_0(\xi,\eta)\, \frac{e^{-ikr_{01}}}{r_{01}^2}\, d\xi\, d\eta, \tag{2.14}$$

where the transverse coordinates (ξ, η) describe the aperture plane and (x, y) the propagated plane. By assuming $U_0 = 0$ outside of Σ, the integration boundaries can be set to infinity.

For the Fresnel (or paraxial) approximation of (2.14), z is assumed to be large in comparison to the transverse field extent, so that r_{01} can be approximated:

$$\begin{aligned} r_{01} &= z\sqrt{1 + \left(\frac{x-\xi}{z}\right)^2 + \left(\frac{y-\eta}{z}\right)^2} \\ &\approx z\left[1 + \frac{1}{2}\left(\frac{x-\xi}{z}\right)^2 + \frac{1}{2}\left(\frac{y-\eta}{z}\right)^2\right]. \end{aligned}$$

by inserting the approximated r_{01} into (2.14), one obtains

$$U(x,y,z) = \frac{ie^{-ikz}}{\lambda z} \iint_{-\infty}^{\infty} U_0(\xi,\eta)\, e^{-\frac{ik}{2z}\left[(x-\xi)^2+(y-\eta)^2\right]}\, d\xi\, d\eta. \tag{2.15}$$

Factoring out the term $e^{-i\frac{k}{2z}(x^2+y^2)}$ yields the *Fresnel diffraction integral*

$$U(x,y,z) = \frac{ie^{-ikz}}{\lambda z}\, e^{-i\frac{k}{2z}(x^2+y^2)} \iint_{-\infty}^{\infty} U_0(\xi,\eta)\, e^{-i\frac{k}{2z}(\xi^2+\eta^2)}\, e^{i\frac{2\pi}{\lambda z}(x\xi+y\eta)}\, d\xi\, d\eta, \tag{2.16}$$

which can be identified, apart from a preceding phase factor, with the two-dimensional inverse Fourier transform of the complex incident field U_0 multiplied with a quadratic phase.

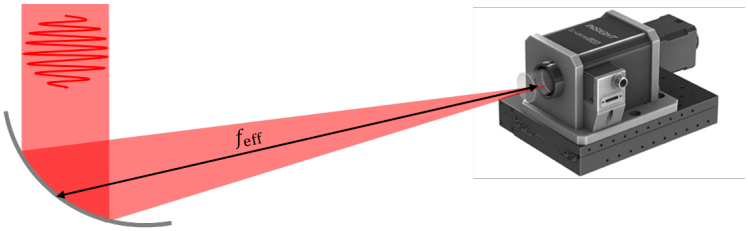

Figure 2.2: Schematic focusing setup: the laser near field is focused by an OAP and reaches the focus position (= far field), where the INSIGHT measurement device is positioned. [17]

Since the Fresnel approximation relies on the replacement of the spherical waves in (2.13) with parabolic wavefronts, its validity depends on the negligibility of higher order phase terms. Therefore, the propagation distance z has to satisfy [16]

$$z^3 > \frac{d^4}{\lambda},$$

where d is the diameter of the aperture Σ. However, if U is truly paraxial, (2.16) also holds for arbitrarily small z.

2.1.4 The Fraunhofer Approximation

If, additionally to the Fresnel approximation condition, the even stronger *Fraunhofer condition*

$$z \gg \frac{k}{2} \cdot (\xi^2 + \eta^2)_{\max} = \frac{\pi}{4\lambda} \cdot d^2$$

is satisfied, implying that the observer is located in the far field of the diffracting element, the quadratic phase factor under the integral of (2.16) is approximately unity and can thus be dropped:

$$U(x,y,z) = \frac{ie^{-ikz}}{\lambda z}\, e^{-i\frac{k}{2z}(x^2+y^2)} \iint_{-\infty}^{\infty} U_0(\xi,\eta)\, e^{i\frac{2\pi}{\lambda z}(x\xi+y\eta)}\, d\xi\, d\eta \tag{2.17}$$

Apart from a preceding quadratic phase factor, this is a simple spatial inverse Fourier transform of the complex field U_0, which is incident on the aperture.

2.1.5 Fourier Transforming Properties of Lenses

The process of focusing a laser field can be described mathematically by a thin spherical lens transformation, although in reality off-axis parabolic mirrors (OAPs) are used for this purpose, since the high intensity of a laser would simply destroy a lens. A corresponding schematic setup can be seen in figure 2.2. The mathematical results of those focusing mechanisms are similar, apart from an additional transverse parity change in the far field introduced by the mirroring process of an OAP.

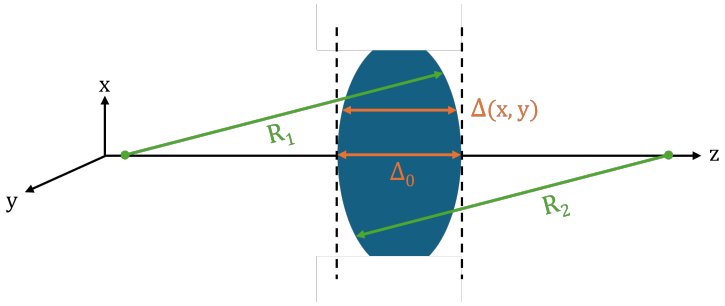

Figure 2.3: Calculating the thickness function Δ of a spherical lens

A thin spherical lens of optically dense material with refractive index n delays an incident wavefront proportionally to its thickness Δ. "Thin" in this context means that the ray translation within the lens is negligible. The total phase delay of a wave passing through such a lens is

$$\phi(x,y) = kn\Delta(x,y) + k(\Delta_0 - \Delta(x,y)).$$

The first term describes the phase delay introduced by the lens and the second term the one by the remaining free space between the two planes enclosing the lens, as indicated in figure 2.3.

Hence, the passage of a complex field U through a thin lens results in a multiplicative phase transformation $U'(x,y) = t(x,y) \cdot U(x,y)$ with

$$t(x,y) = e^{i\phi(x,y)} = e^{-ik\Delta_0}\ e^{-ik(n-1)\Delta(x,y)} \tag{2.18}$$

Neglecting any finite transverse lens extent, the thickness function of a spherical lens can be calculated with

$$\begin{aligned}\Delta(x,y) &= \Delta_0 - R_1\left(1 - \sqrt{1 - \frac{x^2+y^2}{R_1^2}}\right) + R_2\left(1 - \sqrt{1 - \frac{x^2+y^2}{R_2^2}}\right) \\ &\approx \Delta_0 - \frac{x^2+y^2}{2}\left(\frac{1}{R_1} - \frac{1}{R_2}\right),\end{aligned} \tag{2.19}$$

where R_1 and R_2 are the radii of curvature of the lens surface (see fig. 2.3). If both are assumed to be grater than the transverse lens extent ($R^2 \gg x^2 + y^2$), paraxial approximation can be used, as indicated in the second line of (2.19). Inserting (2.19) into (2.18) yields

$$t(x,y) = e^{-ikn\Delta_0}\ e^{ik(n-1)\frac{x^2+y^2}{2}\left(\frac{1}{R_1} - \frac{1}{R_2}\right)}$$

The physical properties of the lens can be combined by the focal length f, which is defined as

$$\frac{1}{f} = (n-1)\left(\frac{1}{R_1} - \frac{1}{R_2}\right),$$

so that the phase transformation can be rewritten as

$$t(x,y) = e^{i\frac{k}{2f}(x^2+y^2)} \tag{2.20}$$

where a constant phase factor has been dropped.

For OAPs, the effective focal length (at the off-axis-section) f_{eff} has to be utilized. Furthermore, transformation factor (2.20) is exact, as OAPs introduce parabolic waves only instead of spherical ones.

After passing a focusing element, the field in the back focal plane (the far field) is obtained by applying the Fresnel diffraction formula (2.16) with $z = f$ to the complex near field distribution $U_{\text{NF}}(x,y,\lambda)$, multiplied with (2.20),

$$U_{\text{FF}}(u,v,\lambda) = \frac{i}{\lambda f}\, e^{-i\frac{\pi}{\lambda f}(u^2+v^2)} \iint_{-\infty}^{\infty} U_{\text{NF}}(x,y,\lambda)\; e^{i\frac{2\pi}{\lambda f}(xu+yv)}\; dx\; dy, \tag{2.21}$$

where it has been assumed that the diameter of the focusing element is greater than the transverse field extent. The constant phase factor e^{-ikf} has been dropped, as it just indicates the time shift introduced by the light to travel the distance f. The quadratic phase factors under the integral cancel out exactly, leaving only a two-dimensional inverse Fourier transform along the two transverse spatial axes (x,y) and an additional quadratic phase factor outside the integral, equivalent to Fraunhofer diffraction (2.17). Thus, the process of focusing corresponds mathematically to a two-dimensional spatial Fourier transform.

Similar results can be obtained when transforming from the mid field, located at a distance $d < f$ in front of the focal plane, to the focal plane. Assuming again parabolic approximation or a parabolic focusing element, a complex field distribution acquires a parabolic phase factor after it. Hence, the mid field distribution can be deducted from the near field with

$$\begin{aligned} U_{\text{MF}}(\xi,\eta,\lambda) &= \frac{f}{d}\, U_{\text{NF}}\left(\xi\frac{f}{d}, \eta\frac{f}{d}, \lambda\right)\; e^{i\frac{\pi}{\lambda d}(\xi^2+\eta^2)} \\ &= U_{\text{MF}}^{\text{flat}}(\xi,\eta,\lambda)\; e^{i\frac{\pi}{\lambda d}(\xi^2+\eta^2)}. \end{aligned} \tag{2.22}$$

The factor f/d arises from the geometric optics approximation, leading to a reduced spot size and, consequently, an increased intensity, in accordance with the principle of energy conservation [15]. Again, the far field distribution is obtained by applying the Fresnel diffraction integral (2.16) to (2.22), where the quadratic phase factors under the integral cancels out again, yielding an inverse spatial Fourier transform:

$$U_{\text{FF}}(u,v,\lambda) = \frac{i}{\lambda d}\, e^{-i\frac{\pi}{\lambda d}(u^2+v^2)} \iint_{-\infty}^{\infty} U_{\text{MF}}^{\text{flat}}(\xi,\eta,\lambda)\; e^{i\frac{2\pi}{\lambda d}(\xi u+\eta v)}\; d\xi\; d\eta \tag{2.23}$$

By inverting (2.23) and multiplying with the missing quadratic phase factor, the mid field distribution can be obtained:

$$U_{\text{MF}}(\xi,\eta,\lambda) = \frac{1}{i\lambda d}\, e^{-i\frac{\pi}{\lambda d}(\xi^2+\eta^2)} \iint_{-\infty}^{\infty} U_{\text{FF}}\left(\frac{u}{\lambda d}, \frac{v}{\lambda d}, \lambda\right)\; e^{i\frac{\pi}{\lambda d}(u^2+v^2)}\; e^{-i\frac{2\pi}{\lambda d}(\xi u+\eta v)}\; du\; dv. \tag{2.24}$$

Please note that the far field needs to be scaled to spatial frequencies $u/\lambda d,\ v/\lambda d$.

2.2 Propagation of Gaussian Pulses

Gaussian beams are widely used in describing and analyzing lasers, since they provide a good approximation to their transverse modes. In its lowest order, the transverse field at the focal plane $z = 0$ follows a simple Gaussian distribution

$$\epsilon_r(r) = e^{-\frac{r^2}{w_0^2}} \tag{2.25}$$

with $r = \sqrt{x^2 + y^2}$. w_0 is the beam waist, where the field amplitude drops to $1/e$ of the value at the pulse center at $r = 0$. The transverse intensity full width half maximum (FWHM) is connected to w_0 via

$$w_{0,\ \mathrm{FWHM,\ I}} = \sqrt{2\ \ln\ 2}\ w_0.$$

Analogously, the spectrum follows a Gaussian distribution around a central frequency ω_0

$$\epsilon_\omega(\omega) = e^{-\frac{(\omega-\omega_0)^2\tau^2}{4}},$$

where τ is the pulse duration, defined as the time when the field amplitude drops to $1/e$ of the maximum value. It is connected to the temporal intensity FWHM via

$$\tau_{\mathrm{FWHM,\ I}} = \sqrt{2\ \ln\ 2}\ \tau$$

The propagated Gaussian pulse is a solution of the Fresnel diffraction integral (2.16) with $U_0(r, \omega) = \epsilon_r(r) \cdot \epsilon_\omega(\omega)$ [16]:

$$E(r, z, \omega) = \frac{w_0}{w(z)}\ \epsilon_\omega(\omega)\ e^{-\frac{r^2}{w(z)^2}}\ e^{-i\left(kz + k\frac{x^2+y^2}{2R(z)} - \arctan\left(\frac{z}{z_R}\right)\right)} \tag{2.26}$$

An exemplary representation can be seen in figure 2.4.

When leaving the focal plane, the beam will diverge away from its waist, which reflects in the waist size $w(z)$, increasing with the propagation distance z:

$$w(z) = w_0\sqrt{1 + \left(\frac{z}{z_R}\right)^2}. \tag{2.27}$$

The *Rayleigh length* $z_R = \pi w_0^2/\lambda_0$ is the typical length scale of a Gaussian beam, after which the beam waist is increased by a factor $\sqrt{2}$.

The wavefront radius of curvature

$$R(z) = z + \frac{{z_R}^2}{z}$$

reverses its sign when passing the focal plane and is infinite there. The curvature is greatest at $z = z_R$.

To switch from spectral to time domain, an one-dimensional inverse Fourier transform (2.7) with respect to ω has to be applied to (2.26), yielding

$$E(x, y, z, t) = E_0\ \frac{w_0}{w(z)}\ e^{-\frac{r^2}{w(z)^2}}\ e^{-\left(\frac{z-ct+\frac{r^2}{2R(z)}}{c\tau}\right)^2}\ e^{-ik\left(z-ct+\frac{r^2}{2R(z)}\right)+i\arctan\left(\frac{z}{z_R}\right)} \tag{2.28}$$

Along the time axis, the the pulse keeps its Gaussian shape.

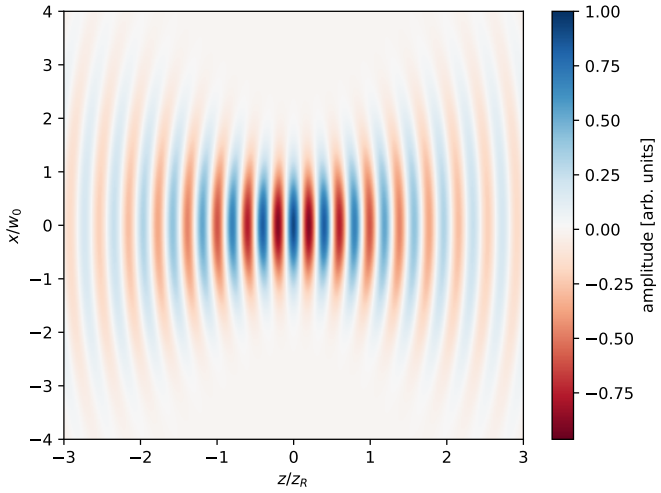

Figure 2.4: Exemplary representation of a propagated Gaussian pulse (real part). When leaving the focal plane at $z = 0$, the pulse starts do diverge as it increases in waist size and drops in amplitude. The curvature of the phase front differs from zero outside $z = 0$ and reaches its maximum at $z = z_R$.

2.3 Dispersion

Realistic laser pulses tend to deviate from the ideal Gaussian shape (2.28). For example, they can exhibit transverse field modulations, which can still be described with higher-order Gauss-Laguerre modes [16]. However, analytic descriptions reach their limits fast when dealing with dispersion, i.e. the dependence of pulse parameters on frequency, and the spatio-temporal couplings (STCs) introduced with these, indicating that temporal and spatial properties cannot be expressed independently from each other anymore. Because small changes in dispersion properties in the near field of ultra-short laser pulses can induce severe pulse distortions around the focus [18] and therefore influence laser-matter interaction profoundly, it is important to include these in realistic simulations.

In the following, the most important dispersion parameters will be introduced:

- **Spatial dispersion** (or spatial chirp) SD is defined as the coefficient of the linear term in the expansion of the transverse field distribution center coordinate x_0 with respect to frequency

$$SD := \left.\frac{dx_0}{d\omega}\right|_{\omega=\omega_0} \tag{2.29}$$

  and leads to an increased beam spot size, as the colors are “smeared out” transversely.

- **Angular dispersion** (or angular chirp) AD is defined as the coefficient of the linear term in the expansion of the beam propagation angle θ with respect to frequency

$$AD := \left.\frac{d\theta}{d\omega}\right|_{\omega=\omega_0}. \tag{2.30}$$

  $\theta(\omega)$ is the angle enclosed by the propagation directions of ω and the central frequency ω_0. The beam propagation direction is defined as $\theta(\omega_0)$, which does not necessarily need to be zero for realistic laser pulses (see chap. 3).

- **Group delay dispersion** GDD (or temporal chirp) is defined as the quadratic order coefficient of the expansion of the spectral phase $\phi(\omega)$ with respect to frequency

$$GDD := \left.\frac{d^2\phi}{d\omega^2}\right|_{\omega=\omega_0}. \tag{2.31}$$

  $\phi(\omega)$ is the phase term of the pulse in the spectral domain. GDD extends the pulse duration, since it spreads the colors out on the time axis: the "red part" of the pulse will reach the focal plane earlier than the "blue part", or vice versa, depending on the sign of GDD [19].

- **Third order dispersion** TOD is defined as cubic order coefficient of the expansion of the spectral phase $\phi(\omega)$ with respect to frequency

$$TOD := \left.\frac{d^3\phi}{d\omega^3}\right|_{\omega=\omega_0} \tag{2.32}$$

  and causes a pre- or post-pulse, since the less intense frequencies right and left from ω_0 arrive earlier or later in time, depending on the sign of TOD [13].

Those dispersion values are interconnected. For example, if AD is present at $z = 0$, the beam will diverge due to the colors travelling into different directions, causing SD at $z \neq 0$. Additionally, if SD or AD are present at $z = 0$, they will contribute to GDD and TOD as the beam propagates [18]. As a consequence, the following relations can be drawn between the dispersion parameters in near and far field of a laser pulse [18]:

$$\begin{aligned} AD_{\mathrm{FF}} &= -SD_{\mathrm{NF}}/f_{\mathrm{eff}} - AD_{\mathrm{NF}} \\ SD_{\mathrm{FF}} &= f_{\mathrm{eff}} \cdot AD_{\mathrm{NF}} \end{aligned} \tag{2.33}$$

This equation holds when an OAP is used to focus the pulse. When utilizing (2.21) to transform between near- and far field, one has to change the sign of (2.33) to compensate for the missing parity change.

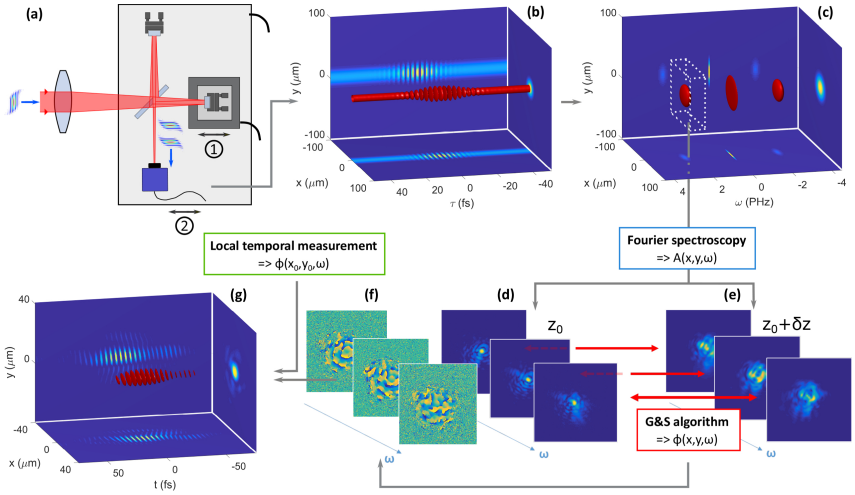

Figure 3.1: Schematic setup and operation principle of INSIGHT. From [20], ©2018 Optical Society of America

3 The INSIGHT Measurement

For the implementation of a realistic laser profile in PIConGPU, accurate measurements of the electric field of a laser pulse are required. For this purpose, INSIGHT provides an ideal measurement technique. The first part of this chapter will be dedicated to the description of the measurement technique, and afterwards the preparation steps will be explained in detail, which are necessary for such a measurement to serve as simulation input.

3.1 Experimental Setup

As suggested by the name, this measurement allows insight into the laser field at the focus position, providing access to the full field information (amplitude and phase) up to an unknown frequency-dependent global phase in the space-frequency domain [17].

The INSIGHT measurement device is placed directly at the focal point of ultrashort laser systems. It mainly consists of a Michelson interferometer (fig. 3.1 (a)), where one arm generates a controllable time delay τ. The outgoing pulses interfere spatially on a camera. Their time delay τ is scanned with sub-optical cycle precision as long as the pulses overlap, and the device measures the resulting spatially-resolved

linear autocorrelation (fig. 3.1 (b))

$$S(x, y, \tau) = \int |E(x, y, t) + E^*(x, y, t - \tau)|^2 d\tau.$$

To obtain the transverse spectral beam intensity profile $\propto E^2(x, y, \omega)$ in the frequency domain, the Fourier transform of S is calculated with respect to the time delay τ (fig. 3.1 (c)). This process is repeated before and after the focus position, typically at a distance of a few Rayleigh lengths. Since the laser phase is encoded in the evolution of the amplitude of $E(x, y, \omega)$ along z, the spatial phase profile at the focus position can be calculated numerically with an iterative Gerchberg-Saxton algorithm, applied separately to each frequency within laser bandwidth (fig. 3.1 (d-f)) [20]. This algorithm is based on the relation between the amplitudes at different z based on a two-dimensional spatial Fourier transform (2.10), so that the spatial phase is retrieved by Fourier-transforming forth and back between those planes and imposing the measured amplitudes at each time step. For that, the measurement of the amplitude at two different z planes would be sufficient, but the usage of three planes increases the stability and accuracy of convergence [20].

While the experimental setup for laser-driven electron acceleration with ultrashort laser pulses at HZDR follows exactly this scheme, the proton acceleration setup does not allow for direct measurements with INSIGHT in the focus, as the measurement is limited downwards with an F-number of $F/10$. The F-number is the effective focal length f_{eff} divided by the transverse beam diameter in the near field and can be used to calculate the beam width in the focus via

$$w_0 = F/\# \cdot \lambda.$$

To achieve relativistic intensities for laser-driven proton acceleration, a F-number of $F/2.3$ is used. Hence, the transverse pulse extent at the focus would be too small to be resolved by the camera, and due to its fast divergence, the pulse will be cropped in the two measurements out of focus. For this reason, the INSIGHT measurement is carried out on a specially for this purpose developed diagnostic setup (fig. 3.2) with $F/42$. This setup generates a "substitute focus" with the same properties as the actual focus, just at different transverse scales. To obtain the real electric field at the actual focus position, a rescaling of the transverse axes with a factor

$$\xi = \frac{1}{10} \cdot \frac{f_{\text{eff, orig}}}{f_{\text{eff, subst}}}$$

must be performed, where 1/10 is the ratio of the demagnification telescope and $f_{\text{eff, subst}}$ is the effective focal length of the substitute focus. Otherwise, all determined parameters are not comparable with the real laser parameters and lead to incorrect results.

Carrying out an INSIGHT measurement is a time-consuming task. Not only the complete target setup (gas nozzle, beam diagnostic tools etc.) needs to be removed

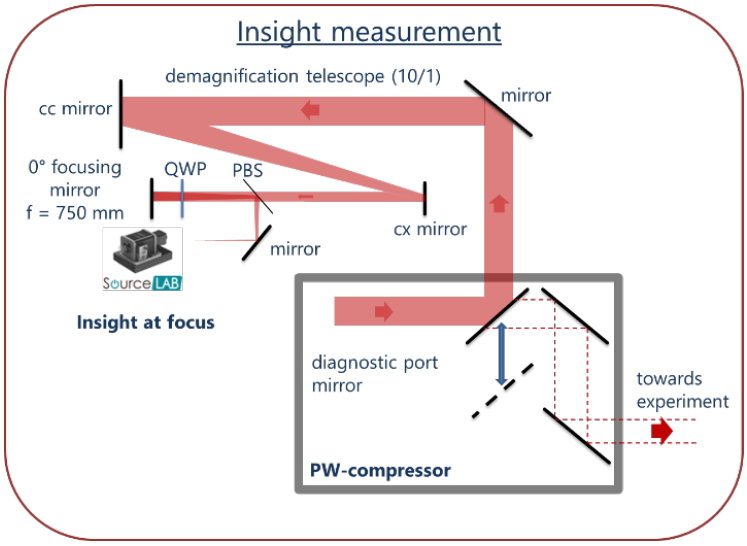

Figure 3.2: Modified INSIGHT setup for laser-driven proton acceleration at HZDR. When the diagnostic port mirror is shifted into the beamline, the laser pulse will be sent through a demagnification telescope with a ratio of 10/1 before being focused. After passing a quarter wave plate (QWP), the polarizing beam splitter (PBS) can select the focused beam and reflect it into the measurement device. ©Thomas Püschel, HZDR

to insert the device, but also many laser shots are necessary to perform the time-delay scan. For a laser system with a pulse repetition rate of 10 Hz, choosing a time window of (typically) $\tau = 200$ fs and $\Delta\tau \sim 0.25$ fs implies an overall measurement time of approximately 4 minutes, depending on the resolution of $\Delta\tau$, whereby the time needed for changing the setup is not included. Nowadays, high-power laser systems for laser-driven particle acceleration tend to have an average pulse repetition rate of 1 Hz. With these systems, the measuring time is increased by a factor of more than ten, and measurement times of 40 minutes are plausible.

Additionally, the processing of many laser shots into one unique result implies measurement of an averaged electric field instead of a single snap shot. The shot-to-shot fluctuations of the laser are thus not represented, and in addition, these can distort the measurement and cause reconstruction artifacts.

Figure 3.3 shows an example INSIGHT measurement of the DRACO Ti:Sapphire chirped pulse amplification laser system at HZDR in the electron cave focused with an OAP ($f_{\text{eff}} = 2$ m), which will be used throughout the following chapters to visualize the further processing steps. Neglecting higher-order transverse modes ("halos") with a relative intensity of up to 10 %, the transverse field can be approximated with a Gaussian distribution (2.25) with a waist size of 18 µm.

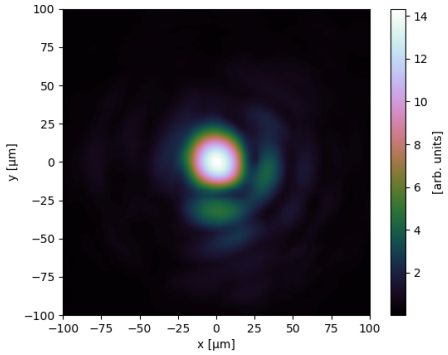

(a) Spectrally integrated amplitude

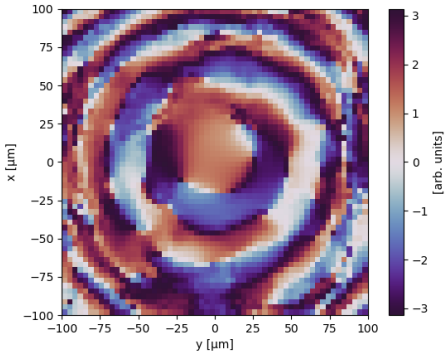

(b) Phase at $\lambda = 799$ nm

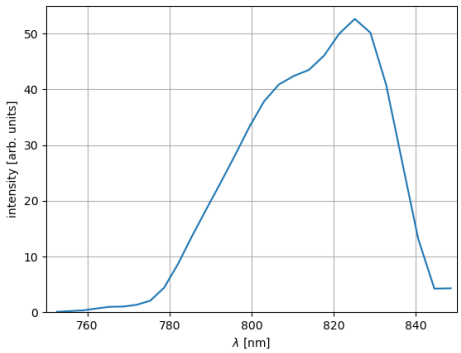

(c) Spectral phase

Figure 3.3: Example INSIGHT measurement of the DRACO laser focal spot at HZDR.

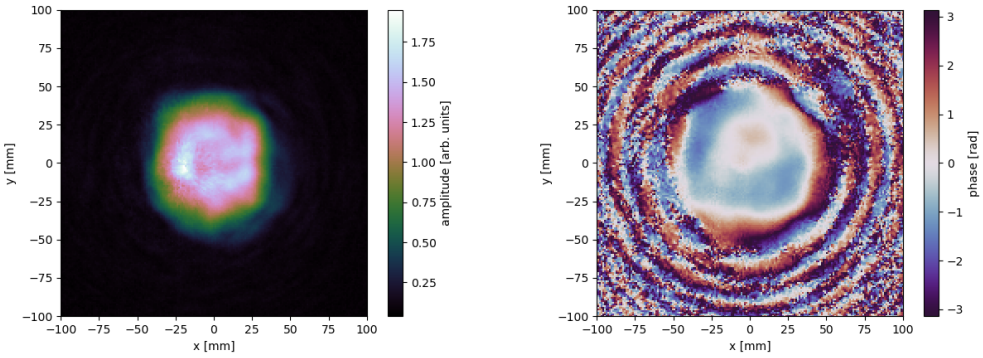

(a) Spectrally integrated near field amplitude (b) Near field phase at $\lambda = 799$ nm

Figure 3.4: Reconstructed near field of the example INSIGHT measurement.

3.2 Analyzing and processing INSIGHT measurements

The necessary processing steps in order to prepare an INSIGHT measurement as simulation input for PIConGPU, will be presented in this chapter. These are implemented in a python script, that forms part of the PIConGPU repository and can be found in [21]. Since this script works independently from any simulation, it can also be used to only visualize and analyze INSIGHT measurements.

3.2.1 Restoring the spectral phase relation

The measurement procedure is blind to the evolution of the phase with frequency, so that the electric field can be obtained only up to a frequency-dependent global phase [20]. This particularly prevents from transforming the measurement into the time domain, since a nonphysical residual spectral phase would cause unwanted dispersive effects. This unknown phase relation can be restored either by an independent measurement of the spectral phase at some position within the laser beamline and subsequent frequency stitching or, if no such measurement is present, by making assumptions onto the beam compression. Only afterwards, the temporal pulse reconstruction is possible.

For the present example data set (see fig. 3.3), no additional spectral phase measurement was available, which is why perfect compression in the near field beam is assumed. This neglects the presence of a residual spectral phase, but it makes the restoration of the spectral phase relation rather straightforward. Therefore, the near field of the pulse is reconstructed by inverting and applying (2.21) with $f_{\text{eff}} = 2$ m to the measured far field, and the result can be seen in figure 3.4.

Perfect beam compression implies a completely flat spectral phase in the near field beam center. Hence, the measured spectral phase in the near field beam center, plotted in figure 3.5, is already the missing spectral phase relation, which consequently has to be subtracted globally from the measured phase. Instead of transforming

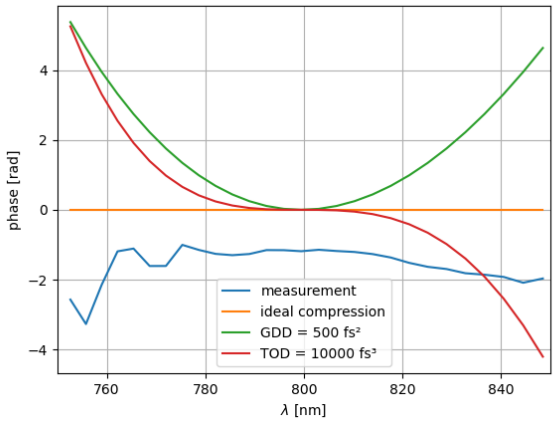

Figure 3.5: The spectral phase in the near field beam center. The measured blue curve corresponds to the missing spectral phase relation when assuming perfect beam compression.

the phase-corrected near field back to the focal plane with (2.21), it is sufficient to subtract the missing spectral phase relation also in the far field, since (2.21) operates on each frequency separately and does not affect global phases.

At this point, phase related dispersion parameters can be added optionally to the pulse, such as GDD (by adding a quadratic spectral phase, see (2.31)), TOD (by adding a cubic spectral phase, see (2.32)) or even higher orders. Some examples are plotted in figure 3.5.

3.2.2 Pulse propagation

In laser-plasma simulations, the laser focus position is typically located somewhere in the simulation volume and not at the beginning of it, where the pulse will be fed in (for details, please refer to chapter 4.2). To fulfill this condition, it is necessary to propagate the measurement out of the focus and back by the distance of the focus position in the simulation volume with respect to the Huygens surface, which generates the incident field and is located close to the simulation volume boundary. To do so, the angular spectrum method (2.12) is applied to every measured frequency, using the two-dimensional discrete Fourier transform algorithm in numpy [22]. An additional phase factor $e^{i\omega z/c}$ is multiplied to the propagated field to cancel out the time shift Δt, which is associated with the propagation distance $z = c \cdot \Delta t$. This ensures that the pulse will always be centered around $t = 0$ in the time domain, which is a useful property when using it as simulation input later on. Since typical PIC-simulations only cover a few millimeters in longitudinal direction, the necessary pulse back-propagation distance is short enough for this method being applicable without reaching its limits or without the need of padding zeros transversely, respectively.

The propagation behaviour of the example INSIGHT measurement in the range $[-2z_R, 2z_R]$ is depicted in figure 3.6. The pulse evolves as expected, as it diverges when leaving the focus. The intensity decreases and the waist size increases in agreement with (2.27). When leaving the focal plane, the pulse looses its transverse Gaussian resemblance. Furthermore, it looks different before and after the focal plane, which can be taken as a hint for the presence of STCs.

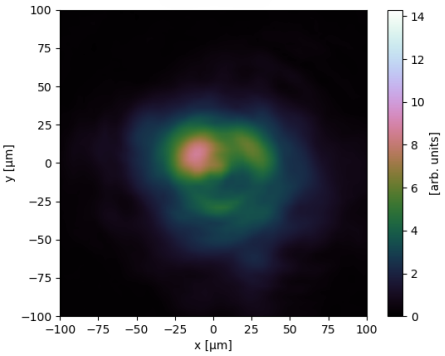

(a) $z = -2z_R$

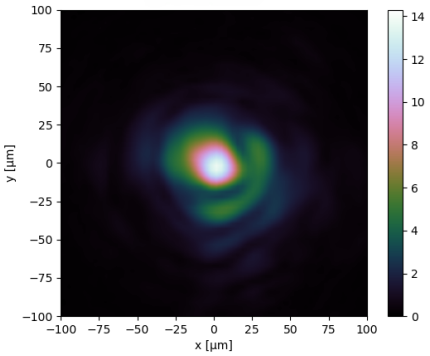

(b) $z = -z_R$

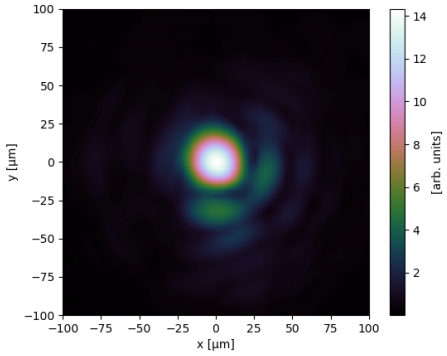

(c) $z = 0$

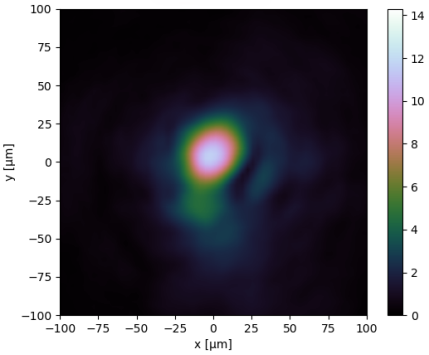

(d) $z = z_R$

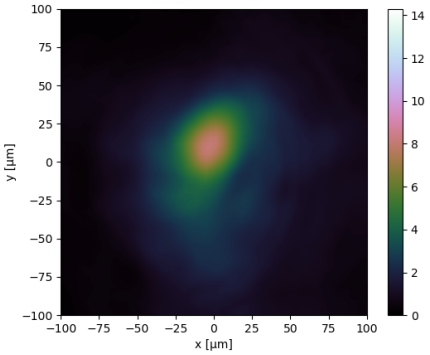

(e) $z = 2z_R$

Figure 3.6: Evolution of the spectrally integrated amplitude of the example INSIGHT measurement along z. The pulse diverges, as it increases in spot size and decreases in intensity ($z_R = 1.28$ mm).

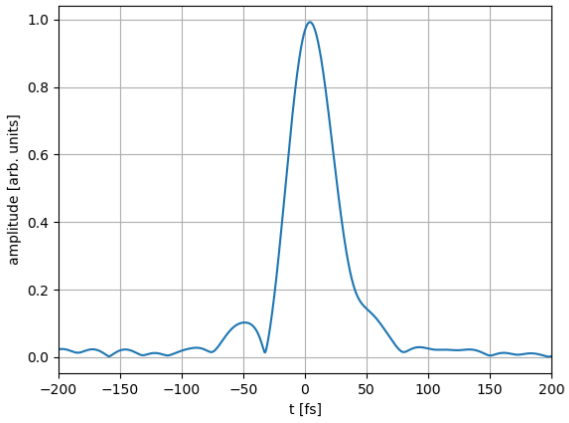

Figure 3.7: Temporal envelope of the example INSIGHT measurement in the pulse center.

3.2.3 Transformation to the time domain

With the restored spectral phase relation and propagated to the desired position, the pulse is ready to be transformed into the time domain, which is required for using it as simulation input. The corresponding inverse Fourier transform along the spectral axis (2.7) is implemented numerically again as a numpy discrete Fourier transform algorithm [22]. By padding zeros before and after the measured spectrum, the measurement can be interpolated onto the desired time step length Δt according to

$$N = \frac{2\pi}{\Delta\omega\ \Delta t},$$

where N is the length of the spectral axis.

The spectrum of the example INSIGHT measurement (fig. 3.3c) exhibits an intensity maximum at 826 nm, which is shifted out of the center of the measurement window from 750 nm - 850 nm. As a consequence, the intensity has not yet dropped to zero at the longer-wavelength boundary. When padding zeros at $\lambda > 850$ nm, still existing (but unknown) fields are probably neglected, and furthermore, a harsh edge in the spectrum is created, which causes sidelobes when Fourier-transforming. Therefore, it is probable that at least part of the sidelobes in the time domain of the example measurement, which are visible in figure 3.7, are non-physical Fourier-transform artifacts.

Extrapolating the measured field to longer wavelengths to restore the missing parts proves to be difficult, because the intensity of the longest measured wavelength (848 nm) is slightly higher than the intensity of the second-to-longest wavelength (844 nm), so that ordinary extrapolation routines lead to diverging intensities. The best choice would be to adjust the measurement interval to longer wavelengths.

If dispersion parameters have been set in the spectral phase correction step (chap.

3.2.1), their effects become visible in the time domain. In the best-compressed case, the example INSIGHT measurement has a pulse duration of $\tau = 26$ fs. GDD increases the pulse duration (fig. 3.8b) and TOD creates a post-pulse (fig. 3.8c).

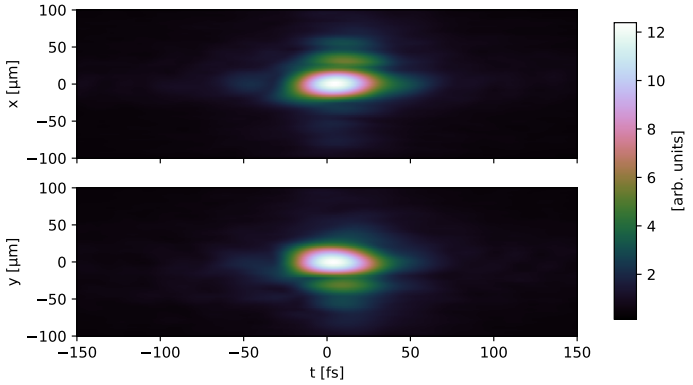

(a) $GDD = 0, TOD = 0$ ($\tau = 26$ fs)

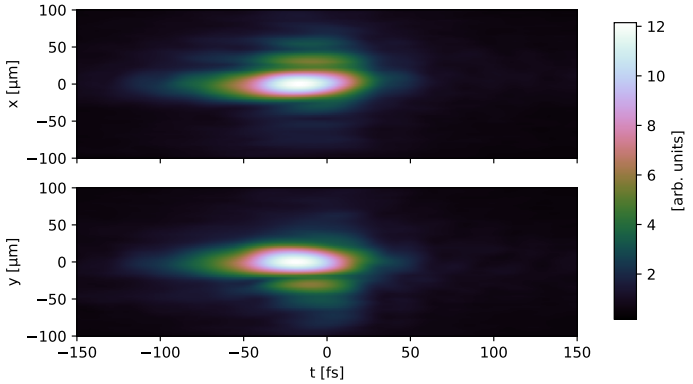

(b) $GDD = 500$ fs^2 ($\tau = 43$ fs)

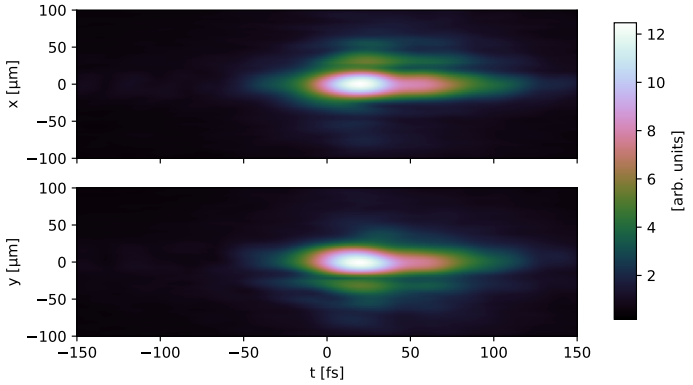

(c) $TOD = 10000$ fs^3

Figure 3.8: Transversely integrated amplitude of the example INSIGHT measurement in the time domain for different dispersion values.

3.2.4 Rescaling the amplitude

Due to stability issues of the phase-restoring algorithm and the omission of energy calibration, the amplitude of an INSIGHT measurement is always normalized to one, independent from the actual pulse intensity. If an additional measurement of the transverse pulse intensity is available, it can be used to rescale the measurement to the actual pulse amplitude; otherwise the pulse energy has to be used.

The pulse energy can be calculated by integrating over the energy density in the whole measured volume

$$W = \iiint_V \frac{\varepsilon_0}{2}(\boldsymbol{E}^2 + c \cdot \boldsymbol{B}^2)\, dV. \tag{3.1}$$

Simplifications are needed to solve this integral.

First, energy conservation allows to change the longitudinal component of the integration volume from $dV = dx\ dy\ dz$ to $dV = dx\ dy\ c\ dt$, since the data set does not depend directly on the longitudinal axis z, but the time axis t.

Second, the electric field $\boldsymbol{E}(x, y, t)$ is assumed to be linearly polarized along the y-direction, as this is the case for the DRACO laser. The other electric field components E_x and E_z were not measured, but they are assumed to be much smaller than the main component E_y anyways, so that $\boldsymbol{E} \approx E_y\, \boldsymbol{e}_y$.

Third, the magnetic field $\boldsymbol{B}$ can be obtained from the third Maxwell equation (2.3) with help of the slowly varying envelope approximation (SVEA) [19]. As the spectral amplitude is centered around a mean frequency $\omega_0 = 2.4$ rad/fs and shows significant intensity only in a frequency interval $\Delta\omega = 0.28$ rad/fs $\ll \omega_0$, it is convenient to introduce ω_0 as carrier frequency and write

$$\boldsymbol{B}(x, y, t) = e^{i\omega_0 t}\boldsymbol{B}_{\text{slow}}(x, y, t),$$

where $\boldsymbol{B}_{\text{slow}}(x, y, t)$ is the complex field envelope. As the name suggests, the temporal variation of the complex envelope within an optical cycle $T = 2\pi/\omega_0$ has to be small to fulfill the inequality $\Delta\omega/\omega_0 \ll 1$:

$$\omega_0|\boldsymbol{B}_{\text{slow}}| \gg \left|\frac{\partial}{\partial t}\boldsymbol{B}_{\text{slow}}\right|.$$

Therefore, the temporal derivative of $\boldsymbol{B}$ in (2.3) can be approximated by

$$\frac{\partial}{\partial t}\boldsymbol{B}(x, y, t) = e^{i\omega_0 t}\left(i\omega_0\boldsymbol{B}_{\text{slow}} + \frac{\partial}{\partial t}\boldsymbol{B}_{\text{slow}}\right) \approx i\omega_0\boldsymbol{B}(x, y, t). \tag{3.2}$$

Inserting into (2.3) yields

$$\boldsymbol{B}(x, y, t) \approx \frac{i}{\omega_0}\nabla \times \boldsymbol{E}(x, y, t),$$

and with $\boldsymbol{E} = E_y\,\boldsymbol{e}_y$ one obtains

$$\begin{aligned} B_x &\approx -\frac{i}{\omega_0}\frac{\partial}{\partial z}E_y \\ B_y &= 0 \\ B_z &\approx \frac{i}{\omega_0}\frac{\partial}{\partial x}E_y \end{aligned} \tag{3.3}$$

The derivative along the longitudinal axis z can be solved again with SVEA, analogously to (3.2), since the oscillation with ω_0 along the temporal axis translates in an oscillation with $k_0 = \omega_0/c$ along the longitudinal axis:

$$\frac{\partial}{\partial z}E_y = e^{-i\frac{\omega_0}{c}z}\left(-i\frac{\omega_0}{c}E_{y,\text{slow}} + \frac{\partial}{\partial t}E_{y,\text{slow}}\right) \approx -i\frac{\omega_0}{c}E_y.$$

Hence,

$$B_x(x,y,t) \approx -\frac{E_y(x,y,t)}{c}. \tag{3.4}$$

The longitudinal magnetic field component B_z can be neglected since $B_x \gg B_z$, as the the electric field E_y varies more slowly along the transverse directions ($\sim w_0 = 18$ µm) than along the longitudinal direction ($\sim \lambda/4 = 0.2$ µm).

With all these considerations, (3.1) finally simplifies to

$$W \approx c \iiint_V dx\; dy\; dt\; \varepsilon_0 E_y^2. \tag{3.5}$$

When applied to the measured electric field in the time domain, a scaling factor for the pulse amplitude E_0 can be obtained, so that the pulse contains the desired energy.

A typical pulse energy of the DRACO laser would be 3 J, corresponding to a normalized laser strength parameter

$$a_0 = eE_0/(k_0 m_e c^2) = 2.4$$

in the case of the present data set.

3.2.5 Pulse dispersion measurement

INSIGHT offers as wavefront analysis tool the decomposition of the spectral phase profile into Zernike polynomials [17]. Such spatio-spectral couplings give a hint on present STCs, as they are their counterpart in the frequency domain [23].

Additionally, SD and AD can be measured by applying (2.29) and (2.30) to the data set, both in the reconstructed near field and the measured far field.

For the AD measurement, the propagation angle θ can be derived from the transverse tilt of the measured phase. The tilt angle α of the phase along the transverse axes is connected to θ by

$$\tan\,\alpha = k \cdot \sin\,\theta \tag{3.6}$$

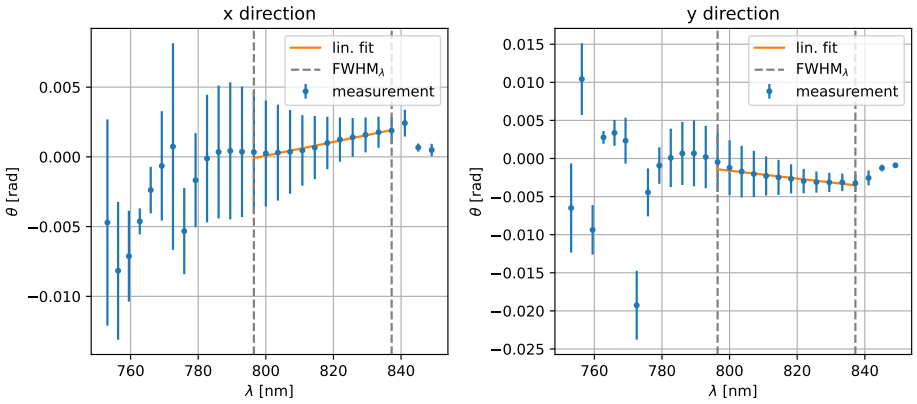

Figure 3.9: Measurement of the propagation angle $\theta(\lambda)$ of the example measurement and linear fit to obtain AD (far field).

or $\alpha \approx k \cdot \theta$ for small angles. The transverse region covering only the main spot of the pulse is selected, within which the transverse phase slope $\tan(\alpha)$ is obtained from a linear fit with the scipy `curve_fit` routine [24] to the phase for every measured wavelength. Outside this region, the phase oscillates too strongly to provide reasonable fit results. The phase slope is transformed into the propagation angle θ with (3.6) and AD can finally be determined by the first-order coefficient of a linear fit to $\theta(\lambda)$, as depicted in figure 3.9. The latter fit is usually only done inside the spectral intensity FWHM, because outside the intensity is too low to obtain significant results, as it can be concluded from the high fluctuation and errorbars in figure 3.9.

The determination of SD results to be more straightforward. The center coordinate of the transverse field distribution in dependence of the wavelength is determined with help of a two-dimensional Gaussian fit in scipy to the pulse intensity at the focus position and as a supergaussian fit of power 2 to the reconstructed near field intensity, since the latter rather follows a flat-top distribution (see fig. 3.4). Again, the slope of a linear fit to the measured center coordinates in dependence of λ inside the spectral FWHM reveals the present SD.

The dispersion values obtained from the INSIGHT measurement are listed in table 3.1. Since no dispersion was applied intentionally onto the pulse, those values correspond to small intrinsic dispersion. The uncertainties were estimated from slight variations of the fitting intervals ($\pm\Delta\lambda$ in the spectral intensity FWHM, $\pm\Delta x$ and $\pm\Delta y$ in the transverse area of maximum intensity), since the uncertainties of the scipy fitting routines were always located several orders of magnitude below the actual fit parameter and underestimated thus the real uncertainty of the dispersion values.

As it can be seen in figures 3.9 and 3.10, a linear fit describes the far field pulse parameters in dependence of λ inside the spectral intensity FWHM well, apart from $y_c(\lambda)$, which exhibits at least a second-order λ-dependence. There, the linear order

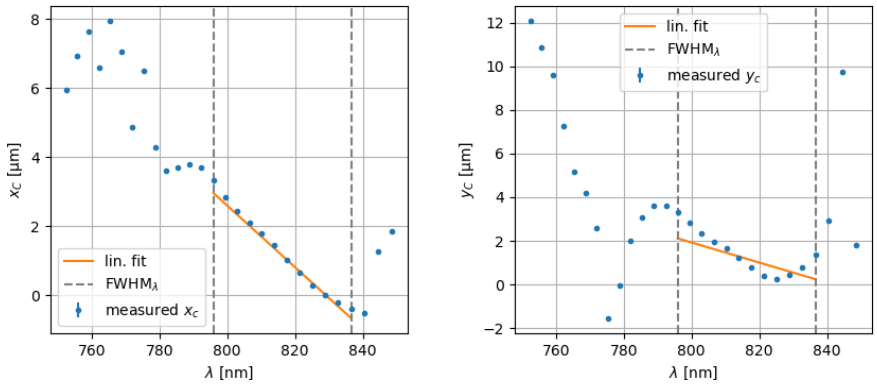

Figure 3.10: Measurement of the pulse center coordinates $x_c(\lambda)$ and $y_c(\lambda)$ and linear fit to obtain SD (far field).

	far field	near field
AD_x [µrad/nm]	49.1 ± 1.4	0.022 ± 0.007
AD_y [µrad/nm]	-54 ± 3	0.052 ± 0.021
SD_x [µm/nm]	-0.091 ± 0.003	67 ± 4
SD_y [µm/nm]	-0.055 ± 0.016	2.1 ± 4.5

Table 3.1: Dispersion values extracted from the INSIGHT measurement.

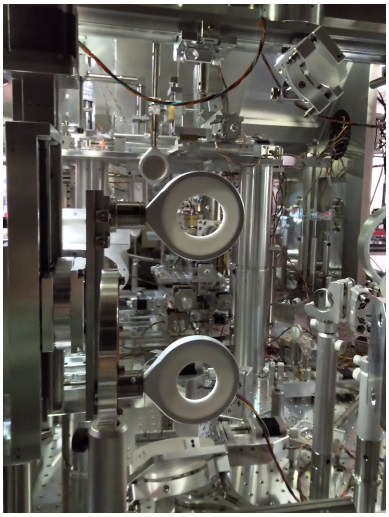

(a) Two different masks installed at the laser beamline.

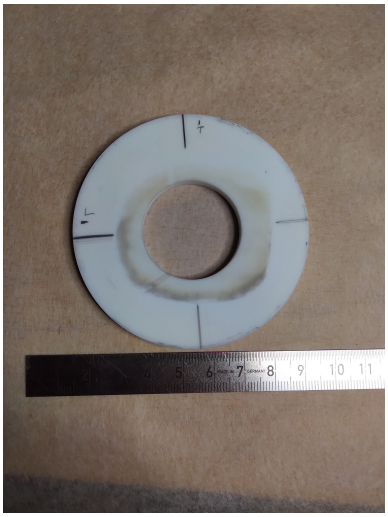

(b) Dismantled mask with a diameter of 32 mm, damaged due to high laser intensity.

Figure 3.11: Masks utilized in the electron cave of the DRACO laser at HZDR.

of (2.29) is not sufficient to describe the measurement exactly.

With the analytic relation between AD and SD (2.33), the obtained dispersion values can be checked for consistency. When taking into account the opposite sign for considering a lens instead of an OAP and using $f_{\text{eff}} = 2$ m, those values are roughly compatible with each other, as they are in the same order of magnitude. Still, the estimated uncertainty is too small to cover the deviation. This can be explained with significantly present higher-order dispersion, which impairs the validity of (2.33).

It has to be emphasized that those dispersion values can be "manipulated", e.g. by changing the slope of the transverse phase $\tan\alpha$ or by shifting the field distribution transversely. One only has to keep in mind the interconnection between the dispersion values of near- and far field and not forget to update the other field with (2.21) after manipulating one of those.

3.2.6 Applying a mask to the beamline

In experiments, masks can be inserted into the beamline to improve beam quality. A corresponding experimental setup can be seen in figure 3.11a. It is possible to simulate the application of such a mask onto an INSIGHT measurement, even if it was initially recorded without mask. To do so, the pulse first has to be propagated back to the mid field at a distance d in front of the focus by applying (2.24). Then, all the field values of those parts of the pulse which would not have passed the mask have to be set to zero, and finally the pulse has to be propagated back to the focal plane with (2.23).

This procedure was applied to the example INSIGHT measurement, utilizing a

circular mask with a diameter of 38.6 mm at a distance $d = 1$ m before the focal plane, analogously to typical experimental setups for electron acceleration at HZDR. The effects of this mask onto the field at the focal plane can be observed in figure 3.12. Compared to the original measurement, it exhibits

- smoothened transverse laser modes and a more radially symmetric appearing field distribution,
- a reduced intensity of higher-order transverse laser modes, such that the maximum halo intensity was lowered from 11 % to 8 % relative to the pulse peak intensity,
- a slightly reduced peak intensity (to 92 %),
- a less quickly oscillating phase outside the main transverse intensity distribution,
- a slightly increased beam waist, from 18 µm to 19 µm, and
- a reduced pulse energy (to 86 %).

The smoothened transverse field distribution becomes even more visible when propagating out of the focus (compare fig. 3.13 to fig. 3.6), and the pulse energy reduction is mainly caused by the field surrounding the main spot transversely, where the mask lowered the amplitude by approximately one order of magnitude (compare figures 3.12c and 3.12d).

When transforming to the time domain, there appears another interesting feature of this virtual mask. As it can be seen in figure 3.14a, the original laser pulse shows a so called “evil side”, where the pulse duration triples in time, from its average 26 fs to nearly 70 fs, which has also been witnessed in experiments at HZDR. Under the influence of the mask, the evil side becomes “less evil”, as it can be confirmed in figure 3.14b: the pulse duration reduces by about 10 fs and also the timing of the maximum intensity crossing the focal plane is aligned better. This can be taken as a first proof that a mask actually improves beam quality.

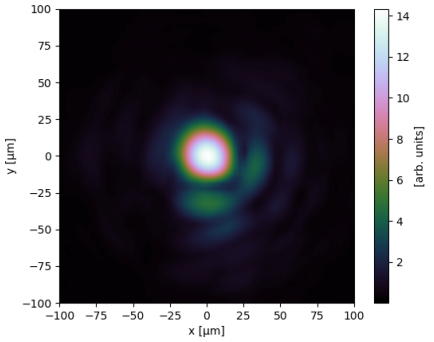

(a) Spectrally integrated amplitude, original measurement

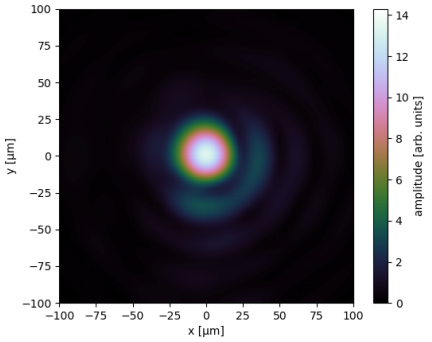

(b) Spectrally integrated amplitude with mask

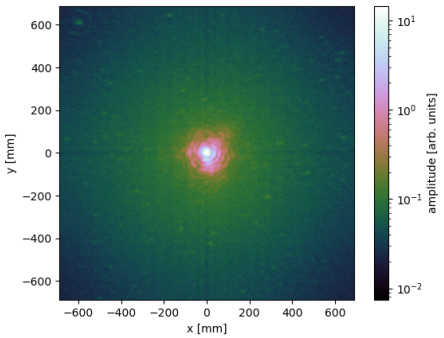

(c) Spectrally integrated amplitude, original measurement, logarithmic

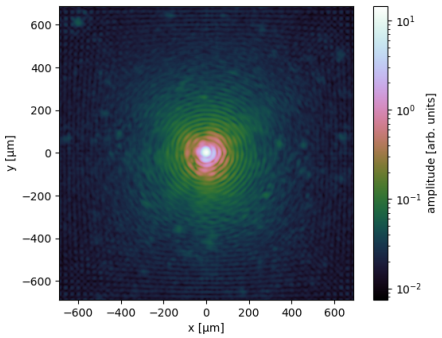

(d) Spectrally integrated amplitude with mask, logarithmic

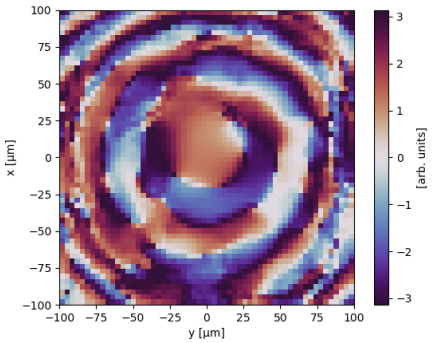

(e) Phase at 800 nm (original)

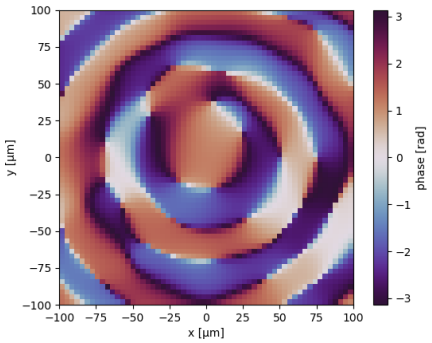

(f) Phase at 800 nm with mask

Figure 3.12: Far field distribution of the INSIGHT measurement with and without applying a mask with a diameter of 38.6 mm at a distance $d = 1$ m before the focal plane.

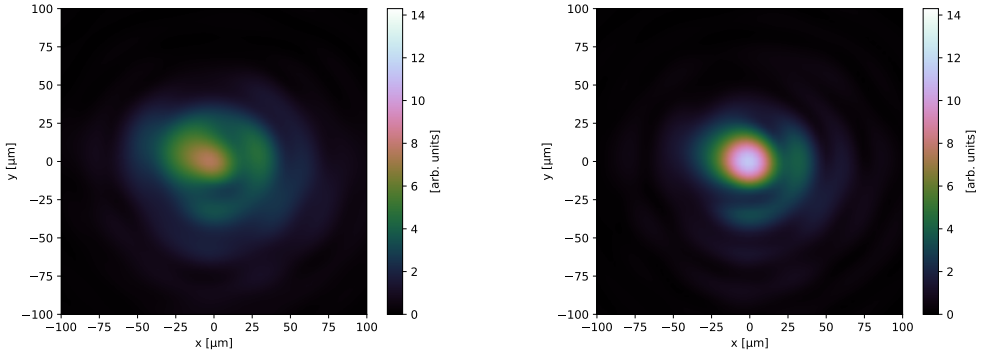

(a) $z = -2z_R$ (b) $z = -z_R$

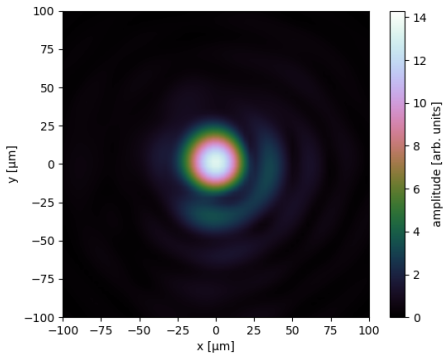

(c) $z = 0$

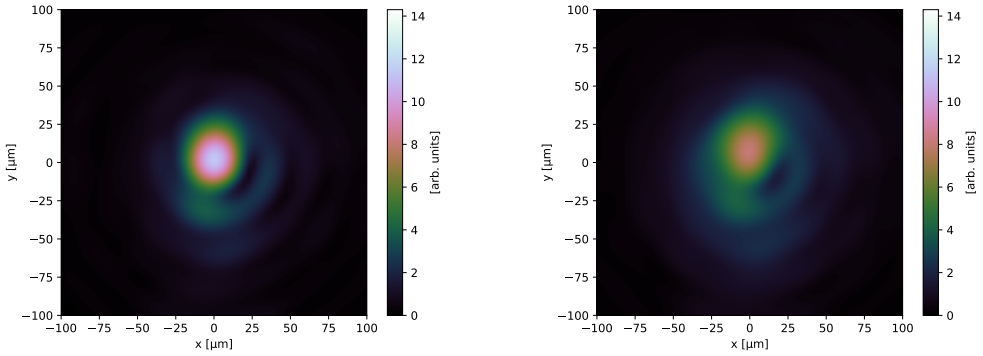

(d) $z = z_R$ (e) $z = 2z_R$

Figure 3.13: Evolution of the spectrally integrated amplitude of the example INSIGHT measurement along z with applied mask ($z_R = 1.28$ mm).

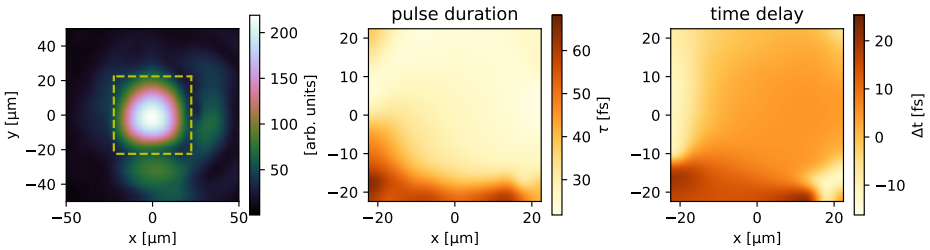

(a) Pulse duration τ and time delay Δt of the original INSIGHT measurement.

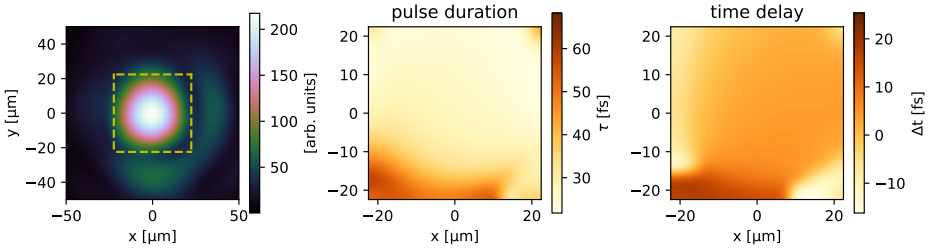

(b) Pulse duration τ and time delay Δt with applied mask.

Figure 3.14: Effects of the mask in the time domain. The yellow square marks transverse area of the maximum pulse intensity, and inside this square the pulse duration τ and the time delay Δt are calculated. Time delay is defined as the point of time when the pulse maximum intensity crosses the focal plane, where the pulse center defines 0.

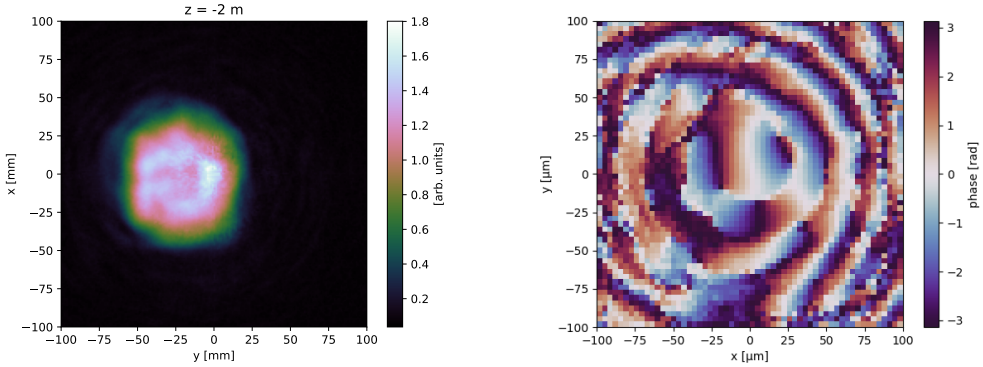

(a) Uncentered spectrally integrated near field (b) Phase at $\lambda = 799$ nm

Figure 3.15: If the near field is shifted out of the center, the far field phase is tilted linearly, which leads to oblique propagation.

3.2.7 Centering the near field

It is useful to center the transverse field distribution of the reconstructed near field, because this avoids oblique propagation of the pulse in the far field.

This connection can be drawn with help of the shift theorem of Fourier transforms [15],

$$e^{i2\pi\nu_0 x} f(x) \quad \overset{\mathcal{F}}{\Longleftrightarrow} \quad \tilde{f}(\nu - \nu_0); \qquad \nu_0 \in \mathbb{R}.$$

Applying this property to (2.21), a shift of the near field distribution out of the center at $x = 0$ by x_c indicates a linear phase tilt at the focus position of

$$U_{\mathrm{NF}}(x - x_c, \lambda) = e^{i2\pi \frac{x_c}{\lambda f} u}\, U_{\mathrm{FF}}(u, \lambda).$$

By inserting the linear phase tilt $\tan\alpha = 2\pi x_c/(\lambda f)$ into (3.6), the offset in propagation direction can be calculated.

In the example measurement, the reconstructed "raw" near field was shifted out of the center by $y_c = -21$ mm (see fig. 3.15a), and the resulting linear phase tilt in the far field, indicating oblique propagation, can be seen in figure 3.15b. A removal of the tilt (fig. 3.3b) and thus straight propagation can be achieved by shifting the near field distribution into the center (fig. 3.4a), and propagating back to the focus position with (2.21).

The precision of the near field shift is limited to its transverse spatial sampling $\Delta x = \Delta y = 1.1$ mm. Thus, a small remaining directional offset in the laser propagation direction cannot be excluded. The uncertainty amounts to

$$\Delta\theta \approx k \cdot \Delta(\tan\alpha) = \frac{\Delta x}{f_{\mathrm{eff}}} = 0.5 \text{ mrad}$$

in the case of the present INSIGHT measurement.

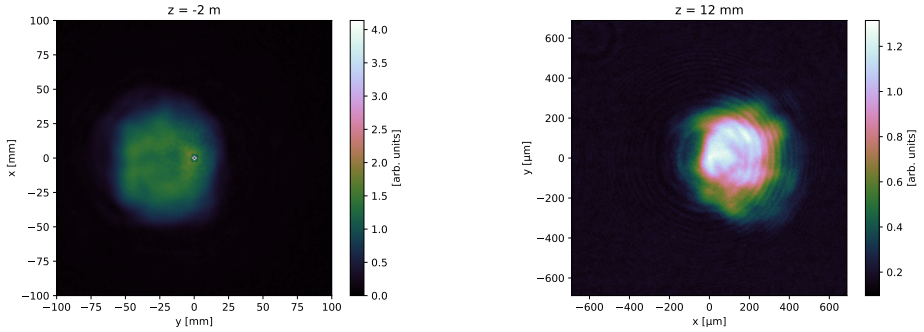

(a) Spectrally integrated reconstructed near field amplitude with artifact at $x = 0, y = 0$.

(b) Spectrally integrated mid field amplitude at $z = 12$ mm. The ring pattern is caused by the peak in the near field.

Figure 3.16: The effects of a non-physical peak in the reconstructed "raw" near field distribution onto the mid field.

This method produces reliable results only for the correction of small deviations of the propagation direction from $\theta = 0°$. The measurement plane is aligned perpendicularly to the propagation direction. Hence, a change in propagation direction would also tilt the measurement plane. As long as this tilt, i.e. the distance Δz to the original measurement plane, stays small, this simplified approach of changing only the propagation direction while keeping the original measurement plane is justified. For the present INSIGHT measurement, $\theta \approx y_c/f_{\text{eff}} = 11$ mrad, and $\Delta z = w_0 \cdot \tan\theta = 0.19\ \mu\text{m} < \lambda_0 = 0.8\ \mu\text{m}$, which confirms that the change in propagation angle is small enough for the manipulated measurement to continue being valid.

3.2.8 Further processing steps

Because of the complicated measurement procedure, depending on many laser pulse shots, which vary slightly (and up to now uncontrollably) over time, INSIGHT measurements seem to be prone to measurement artifacts, which have to be compensated for.

For example, the here presented example measurement exhibited a non-physical peak in its reconstructed near field distribution, which is visible in figure 3.16a. This peak causes ring-shaped disturbances in the mid field (see fig. 3.16b). These can be avoided by smoothening the near field distribution. Therefore, the peak is cut out and the resulting hole is filled with field values interpolated from its surroundings, before propagating the corrected version of the near field (fig. 3.15a) back to the focal plane with (2.21).

As a final step, the prepared electric field $\boldsymbol{E}(\boldsymbol{r}, t)$ has to be saved to openPMD, an open meta-data scheme that is used to store simulation data in PIConGPU, as it provides meaning and self-description for data sets [25].

3.3 Cross-checking and validating the processing methods

3.3.1 Comparing propagated fields

An intermediate product of INSIGHT measurements is the transverse intensity distribution a few millimeters before and after the focus. Those can be compared to the intensity distribution obtained by numerically propagating the pulse out of the focus to the intermediate measurement planes with (2.12), to confirm that numerical propagation takes place in the correct direction. In contrast to completely symmetric Gaussian pulses (2.28), realistic laser pulses tend to look differently before and after the focus due to the presence of STCs. Hence, in laser-plasma simulations it is relevant which side of the focus interacts with the plasma and propagating "backwards" would provide wrong results. The intensity distributions at $z = \pm 3$ mm obtained as intermediate products during the example INSIGHT measurement exhibit different substructures, e.g. a ring pattern at $z = -3$ mm (figs. 3.17a, 3.17c) with a diameter of ~ 50 µm, which is not continuous in its upper left part but intensity-peaked in its lower right part, or a more Gaussian-like but diagonally smeared intensity peak at $z = +3$ mm (figs. 3.17b, 3.17d). These substructures allow to visually identify the intermediate measurement results with the numerically to $z = \pm 3$ mm propagated pulses, so that the correct propagation behaviour can be confirmed.

Additionally, the consistency of the two used propagation mechanisms, angular spectrum (2.12)) and Fresnel diffraction (2.21), was investigated. Due to memory capacity issues, it is not possible to propagate from the focus position to the near field of the pulse. However, it can be worked with the implication of (2.22), that for propagation distances $z \gg w_0$ out of the focus, the resulting mid field intensity distribution looks similar to the near field, only at smaller transverse scales. For this purpose, the example INSIGHT pulse has been propagated to the mid field at $z = -35$ mm with the angular spectrum method (2.12) (see fig. 3.18a). Since the pulse divergence at this distance was too big to fit into the original measurement window, it had to be increased by padding zeros transversely. Specific structures in the spectrally integrated amplitude of figure 3.18, such as a weak halo at the upper left pulse edge, an intensity peak at $(x = 0, y = 0)$ and a hole in the beam center, allow to confirm the similarity of mid- and near field visually. Additionally, it has been worked with the uncentered near field (chap. 3.2.7), so that the shift out of the transverse window center into the left half of the transverse window provides another reference point. Furthermore, the measured beam waist scales according to the scaling law indicated in (2.22)

$$\frac{f_{\text{eff}}}{z} \approx \frac{w_{\text{NF}}}{w_{\text{MF}}} \approx 59$$

This confirms the validity of (2.22) and thus indirectly also the consistency of the two used propagation mechanisms.

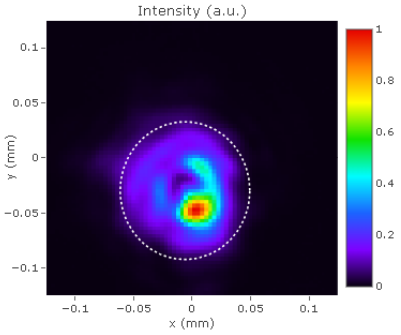

(a) Spectrally integrated intensity 3 mm before the focal plane (INSIGHT)

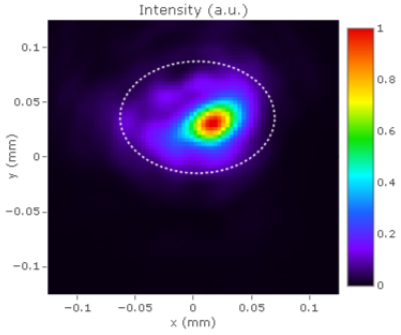

(b) Spectrally integrated intensity 3 mm after the focal plane (INSIGHT)

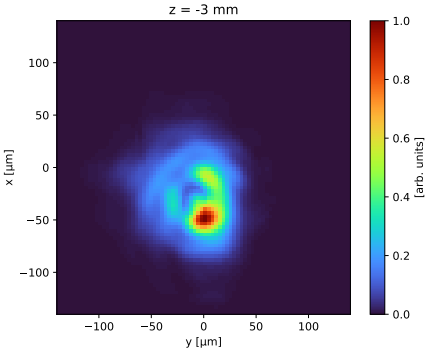

(c) Spectrally integrated intensity, numerically propagated to $z = -3$ mm

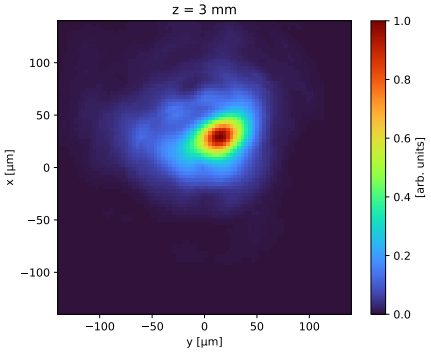

(d) Spectrally integrated intensity, numerically propagated to $z = +3$ mm

Figure 3.17: Comparing the measured intensity distribution 3 mm before and after the focal plane with the numerically propagated results. The field distributions can be identified visually with each other. Please note that the naming of the coordinate axes is transposed.

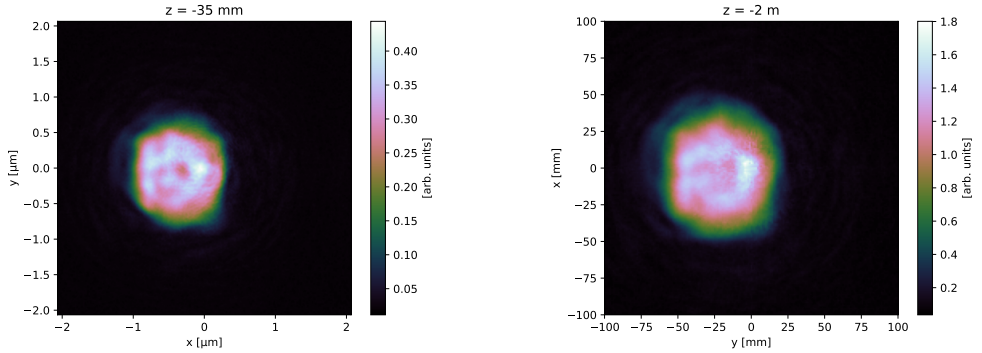

(a) Spectrally integrated mid field amplitude at $z = -35$ mm ($w = 0.73$ mm)

(b) Spectrally integrated near field amplitude (at $z = f_{\text{eff}} = -2$ m, $w = 43$ mm)

Figure 3.18: After a propagation distance $z \gg w_0$, the transverse mid field intensity looks similar to the near field, but at smaller scales)

3.3.2 Pulse energy calculation

The third Maxwell equation (2.3) can be solved exactly, without using SVEA, in the spatial frequency domain. Therefore, the fields are transformed with an inverse two-dimensional Fourier transform (2.10), whereby spatial derivatives are replaced by a factor $-i\boldsymbol{k}$, analogously to the factor $i\omega$ substituting for temporal derivatives in the spectral domain:

$$-i\boldsymbol{k} \times \hat{\tilde{\boldsymbol{E}}}(\omega, \boldsymbol{k}) = -i\omega \hat{\tilde{\boldsymbol{B}}}(\omega, \boldsymbol{k}).$$

With $\boldsymbol{E} = E_y\, \boldsymbol{e}_y$, the magnetic field components are

$$\begin{aligned} \hat{\tilde{B}}_x &= -\frac{k_z}{\omega} \hat{\tilde{E}}_y = -\frac{\sqrt{\left(\frac{\omega}{c}\right)^2 - k_x^2 - k_y^2}}{\omega} \hat{\tilde{E}}_y \\ \hat{\tilde{B}}_y &= 0 \\ \hat{\tilde{B}}_z &= \frac{k_x}{\omega} \hat{\tilde{E}}_y \end{aligned} \tag{3.7}$$

To the obtain magnetic field in the spatial domain, a two-dimensional Fourier transform has to be applied with respect to k_x and k_y.

The relative amplitude difference between the approximated (3.4) and the correctly calculated (3.7) transverse magnetic field component B_x of the example INSIGHT measurement is of the order 10^{-4}, as it can be seen in figure 3.19. Since this difference is negligibly small, it was decided to use the approximated solution for the pulse energy calculation, as it implies less computational effort.

The longitudinal field component B_z can be neglected in the energy calculation, as both approximated and correctly calculated results are much smaller than the

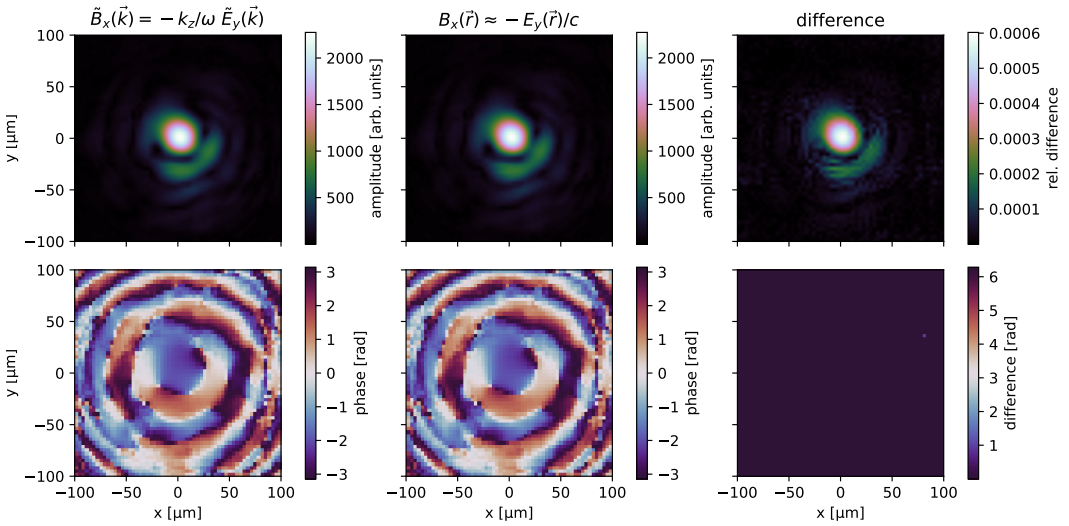

Figure 3.19: Comparing the correctly calculated (3.7) transverse magnetic field component B_x to the solution approximated with SVEA (3.4). The relative difference is negligibly small. All plots at $\lambda = 799$ nm.

transverse magnetic field component B_x. In the case of the example INSIGHT measurement, its relative intensity was approximately 0.007, as it can be obtained from figure 3.20. The intensity of the longitudinal magnetic field component will increase if the spot size w_0 decreases, as it scales with the transverse spatial derivative of the electric field; but even a smaller spot size w_0 of ~ 2 µm, which is used for proton acceleration at HZDR, would still fulfill the condition $w_0 \gg \lambda/4$ and therefore $B_x \gg B_z$. With respect to the example measurement, reducing the spot size to $w_0/10$ elevates the amplitude of B_z by one order of magnitude, which would still be clearly below the amplitude of B_x. Thus, omitting the longitudinal magnetic field component when calculating the pulse energy will not cause significant deviations in any case.

To analyze the impact of the integration variable change from dz to $c\ dt$, the energy content of a simple Gaussian pulse (2.28) similar to the example INSIGHT measurement was calculated , i.e. $\tau = 26$ fs, $\lambda_0 = 800$ nm, $w_0 = 18$ µm while using a similar window extent and resolution. The relative difference between integrating along the longitudinal axis and along the temporal axis, multiplied by c, was of the order of 10^{-5}, independently of the longitudinal grid resolution, and arises due to numerical and discretisation errors. However, it grows with a smaller beam waist, for example to the order of 10^{-3} for $w_0 = 2$ µm. A smaller beam waist implies faster beam divergence, which will exhibit visible effects along the longitudinal axis in the integration volume for sufficiently small values ($c\tau/z_R \sim 1$). With a constant grid resolution, this increases the discretisation error, since the pulses look differently along longitudinal and temporal axis in this case.

An up to now unknown value is the signal-to-noise ratio (SNR) of the INSIGHT

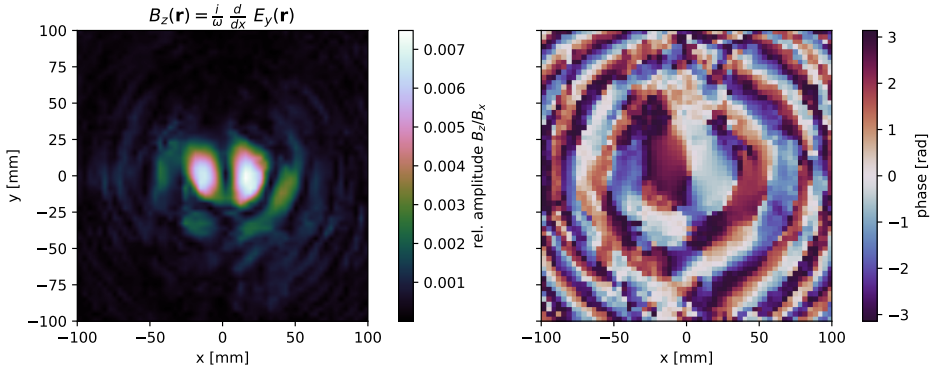

Figure 3.20: The longitudinal magnetic field component B_z, calculated with SVEA (3.2). Its amplitude is more than two orders of magnitude below the transverse component B_x (fig. 3.19).

measurement device. Remaining noise in the data set would have an impact on the pulse energy calculation, since those values do not contribute to its energy content. By interpreting (3.1) as integration over the entire measurement volume, the absence of background noise is assumed, equivalent to the entire measured field being part of the laser pulse, which may lead to an underestimation of the actual pulse amplitude. However, the deviation to the case of possibly present noise should be reasonably small, as the main intensity spot of the pulse contributes to 95 % of the energy content of the measurement window, and the surrounding area only to the remaining 5 %.

3.3.3 Effects of a mask

Similarly to the restoration of the pulse amplitude, calculating the effects of a mask is carried out assuming the absence of noise in the measurement device due to the unknown SNR. This may lead to a slight overestimation of the calculated energy reduction, because setting the affected field values to zero assumes that these are part of the pulse and not noise in the measurement device. Additionally, the extent of the virtual mask is assumed to be infinite, but its experimental counterpart is finite with a total extent of about 80 mm (see fig. 3.11b), which is why setting all the field values apart from the mask aperture to zero may not be completely justified.

However, in experiments at the DRACO laser, where the real counterpart of the virtual mask has been inserted into the beamline (d = 38.6 mm, 1 m before the focal plane), an energy decrease to about 85 % of the initial value has been reported, similar to effects of the virtual mask. Also the other mentioned effects of a virtual mask onto the laser focal spot distribution were reported to be similar in corresponding experiments, such as an increase in spot size, a reduced halo intensity and a change in the transverse modes. Thus, it can be concluded, that the effects of

a mask on INSIGHT measurements are calculated correctly (chap. 3.2.6), despite the simplifying assumptions and the unknown SNR.

4 Including the INSIGHT measurement as new pulse profile into PIConGPU

4.1 The PIC algorithm

PIConGPU is a fully relativistic, manycore, 3D3V and 2D3V particle-in-cell (PIC) code, being developed at HZDR [26]. The underlying algorithm is a key technique in computational plasma physics. It simulates the behavior of a plasma by calculating the motion of its electrons and ions in the present electromagnetic fields with the Vlasov-Maxwell equation [10]:

$$\frac{\partial}{\partial t} f_s(\boldsymbol{x}, \boldsymbol{p}, t) + \boldsymbol{v} \cdot \nabla_x f_s(\boldsymbol{x}, \boldsymbol{p}, t) + q_s \left[\boldsymbol{E}(\boldsymbol{x}, t) + \frac{\boldsymbol{v}}{c} \times \boldsymbol{B}(\boldsymbol{x}, t) \right] \cdot \nabla_p f_s(\boldsymbol{x}, \boldsymbol{p}, t) = 0 \quad (4.1)$$

The velocity $\boldsymbol{v}$ of a particle of species s is connected to its momentum by

$$\boldsymbol{v} = \frac{c\,\boldsymbol{p}}{\sqrt{(m_s c)^2 + |\boldsymbol{p}|^2}}.$$

As the number of particles involved in typical plasma simulations is usually extremely large, they are combined to so-called *macroparticles*, which can contain up to millions of particles of a species s. Since the Lorentz force only depends on the charge-to-mass ratio q_s/m_s, a macroparticle follows the same trajectory as an individual particle of the same species would. The distribution of these macroparticles is described by the function f_s and tracked in a continuous 6D phase space ($\boldsymbol{r}$, $\boldsymbol{p}$), whereas the fields $\boldsymbol{E}$ and $\boldsymbol{B}$ are stored on the grid nodes of a regular Eulerian (stationary) mesh, which discretizes the simulation volume. f_s is calculated from the initially delta-distributed macroparticles with help of an assignment function $W(\boldsymbol{x})$, which assigns their charge to neighbouring mesh points [27]:

$$f_s = \frac{1}{\Delta V} \sum_i q_i W(\boldsymbol{x}_i - \boldsymbol{x}) \delta(\boldsymbol{v}_i - \boldsymbol{v})$$

A schematic illustration of this procedure is shown in figure 4.1. The temporal evolution of f_s is simulated by advancing the macroparticles over time according to (4.1).

The temporal evolution of the fields $\boldsymbol{E}$ and $\boldsymbol{B}$ is computed with the Finite-Difference Time-Domain (FDTD) method [28], suggesting that the partial space and time derivatives occurring in Maxwell's equations are approximated by centered finite differences. In this approach, the derivatives of field values are computed at

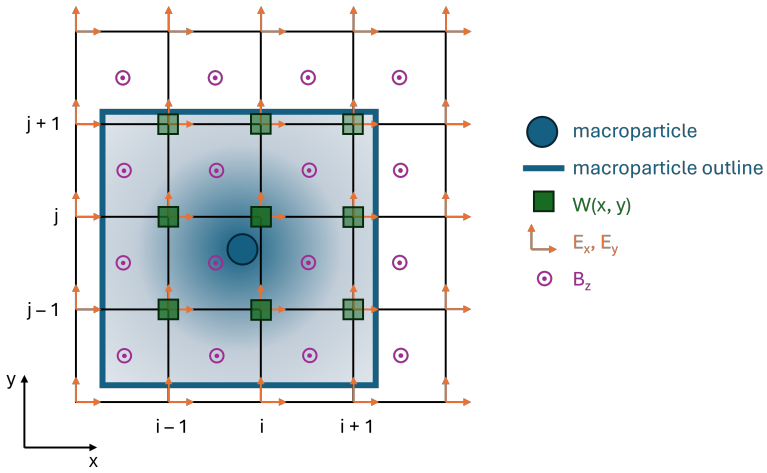

Figure 4.1: Charge assignment of a macroparticle to neighbouring grid points.

positions intermediate to those where the field values are explicitly known. This results in a staggered grid arrangement, where the electric and magnetic field are offset by half a grid cell in space and half a time step (see fig. 4.1).

The basic PIC cycle, representing a single simulation time step ($n \to n+1$), comprises four consecutive steps, which are computed for all particles involved in the simulation:

1. Interpolating the fields $\boldsymbol{E}^n, \boldsymbol{B}^n$ onto the particle position $\boldsymbol{x}^n$ with help of the assignment function W.

2. *Particle push:* By integrating the equation of motion obtained from the Lorentz force acting on the macroparticle, its change in position $\boldsymbol{x}$ and velocity $\boldsymbol{u} = \gamma \boldsymbol{v}$ is obtained:

$$\boldsymbol{u}^{n+3/2} = \boldsymbol{u}^{n+1/2} + \Delta t \frac{q}{m}(\boldsymbol{E}^n + \bar{\boldsymbol{v}}^n \times \boldsymbol{B}^n)$$
$$\boldsymbol{x}^{n+1} = \boldsymbol{x}^n + \Delta t \; \boldsymbol{u}^{n+1/2}$$

   $\bar{\boldsymbol{v}}^n$ is an approximated velocity at $t = n$.

   There exist various particle pushers, each offering different approximation schemes for $\bar{\boldsymbol{v}}^n$ [29]. They differ in accuracy and performance, but all are computationally intensive:

   - the **Boris pusher**, which is phase space volume- and energy-preserving, but the latter only for a vanishing electric field. However, the errors introduced with $\boldsymbol{E} \neq 0$ are usually negligible. Additionally, it looses accuracy in the highly relativistic regime and does not compute the $\boldsymbol{E} \times \boldsymbol{B}$ velocity correctly[30].

- the **Vay pusher**, which was designed to preserve the $\boldsymbol{E} \times \boldsymbol{B}$ drift, but conserves neither energy nor phase space volume strictly. However, it operates in many applications up to a satisfactory level [29].
- the **Higuera–Cary pusher**, which is phase space volume-preserving and resolves the $\boldsymbol{E} \times \boldsymbol{B}$ motion correctly. It is not strictly energy-conserving, but operates with more accuracy than the Boris and Vay method [29].

3. *Current deposition*: The current caused by the macroparticle movement can be computed by solving the continuity equation of electrodynamics with Esirkepov's method [31], which is exactly charge conserving:

$$\rho^{n+1} = \rho^n + \Delta t \cdot \nabla \boldsymbol{J}^{n+1/2}$$

The charge densities ρ^n, ρ^{n+1} can be obtained from the macroparticle position before and after movement with help of the assignment function W. With that, $\boldsymbol{J}$ can be computed.

A major part of the computation time of one PIC iteration is spent on the current deposition stage, such that an overall performance increase can be achieved by utilizing the more efficient EZ (*Esirkepov meets ZigZag*) method [32].

4. *Field update*: By inserting the current $\boldsymbol{J}$, the electromagnetic fields can be updated with the third and fourth Maxwell equation ((2.3), (2.4)) [28]:

$$\begin{aligned}
\boldsymbol{B}^{n+1/2} &= \boldsymbol{B}^n - \frac{\Delta t}{2} \nabla \times \boldsymbol{E}^n \\
\boldsymbol{E}^{n+1} &= \boldsymbol{E}^n + c^2 \Delta t \left(\nabla \times \boldsymbol{B}^{n+1/2} - \mu_0 \boldsymbol{J}^{n+1/2} \right) \\
\boldsymbol{B}^{n+1} &= \boldsymbol{B}^{n+1/2} - \frac{\Delta t}{2} \nabla \times \boldsymbol{E}^{n+1}
\end{aligned}$$

The update of the magnetic field is split in two updates of half a time step, so that electric and magnetic field are known at equal time $t = n + 1$, which is necessary for the particle pusher input [33].

By running the cycle multiple times, a longer simulation duration is achieved.

The field update requires only information from neighbouring or next-to neighbouring cells, depending on the FDTD scheme involved. This locality allows a parallelized computation of the algorithm by sub-dividing the simulation volume and mapping the underlying mesh onto local memory subsets, which can then be assigned to a single processing unit (see fig. 4.2). Data transfer between processing units is required at every time step to transfer field data between neighbouring cells and when particles cross cell boundaries [34].

Since graphical processing units (GPUs) are designed for parallel data processing, they serve as ideal tool to solve the PIC algorithm. PIConGPU was the first scalable GPU cluster implementation of the PIC algorithm in plasma physics [34], where

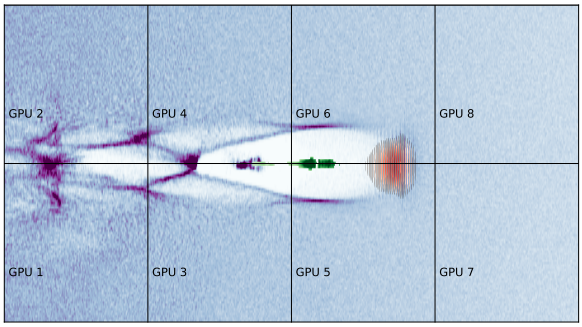

Figure 4.2: Dividing the simulation volume in subdomains. Here, these are calculated in parallel by GPUs.

GPUs carry the main load of the simulation and central processing units (CPUs) are only necessary for communication among the involved GPUs. Nowadays, however, PIConGPU is also able to run fully on CPUs, ARM-processors and other processing units by utilizing the abstract parallel C++11 kernel acceleration library *alpaka* [35].

Due to the approximations introduced with the FDTD scheme, the numerical dispersion relation will differ from the real one. It relates the wave vector $\boldsymbol{k}$ with the angular frequency ω, and in vacuum it reads

$$\omega^2 = (c \cdot \boldsymbol{k})^2.$$

The simplest FDTD scheme is the *Yee* field solver [36], which uses only nearest neighbours and second-order finite differences for the approximation of spatial derivatives. With that, the dispersion relation changes to

$$\omega = \frac{2}{\Delta t} \arcsin(\xi)$$

with

$$\xi = c\Delta t \sqrt{\left[\frac{1}{\Delta x}\sin\left(\frac{k_x \Delta x}{2}\right)\right]^2 + \left[\frac{1}{\Delta y}\sin\left(\frac{k_y \Delta y}{2}\right)\right]^2 + \left[\frac{1}{\Delta z}\sin\left(\frac{k_z \Delta z}{2}\right)\right]^2}.$$

ξ is limited by

$$\xi_{\max} = c\Delta t \sqrt{\frac{1}{\Delta x^2} + \frac{1}{\Delta y^2} + \frac{1}{\Delta z^2}} \leq 1, \tag{4.2}$$

where the condition $\xi_{\max} \leq 1$ has to be fulfilled for the field solver to operate stably. Typically, $\xi_{\max} = 0.995$ is chosen [33], which relates the time sampling Δt with the grid resolution $(\Delta x, \Delta y, \Delta z)$.

Furthermore, the modified dispersion relation implies an anisotropy in phase velocity $v = \omega/k$. The best result (i.e. close to c) is obtained for diagonal propagation,

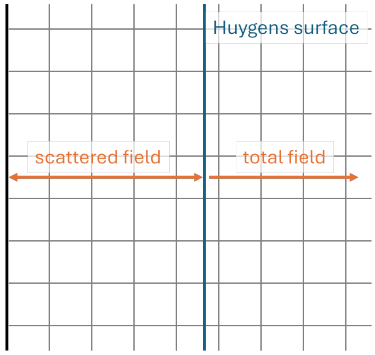

Figure 4.3: Schematic position of the Huygens surface in the simulation volume and region of total and scattered field.

and the error is largest for propagation along the cell edges. This field solver dispersion can be reduced by increasing the grid sampling or including higher orders in the finite difference approximation [33].

4.2 The incident field method

Fields produced by external sources, such as lasers, are fed into a PIConGPU simulation using the *Total Field/Scattered Field* (TF/SF) technique [28], which is implemented in PIConGPU as *incident field method* [37].

Based on the linearity of Maxwell's equations, the total field can be decomposed in incident and scattered field, where the latter results from interaction of the incident field with any obstacles in the simulation volume. Maxwell's equations hold separately for both total and scattered field, which allows to virtually subdivide the simulation volume with an axis aligned *Huygens surface* into an inner core and an outer shell, as shown in figure 4.3. The Huygens surface is thereby chosen in a way that no grid nodes lie on it, located close to the simulation volume boundary but shifted inwards by a user-defined position in full cells and an additional 0.75 cells [37]. In the inner core of the simulation volume (right of the Huygens surface in figure 4.3), only total field is present, whereas in the outer shell (left of the Huygens surface in figure 4.3), only scattered field is present. Thus, the incident field is generated at the Huygens surface and propagates into the simulation volume. To ensure the preservation of total and scattered fields in their respective regions and thus the correct generation of the incident field, the field solver update has to be modified in those regions, where field values were calculated using a mix of total and scattered field. This corresponds to a single layer located near the Huygens surface. Either, the incident field has to be added to the scattered field or subtracted from the total field. Physically, this corresponds to a virtual current sheet on the Huygens surface generating the incident field, which then propagates into the inner core of the simulation volume [38].

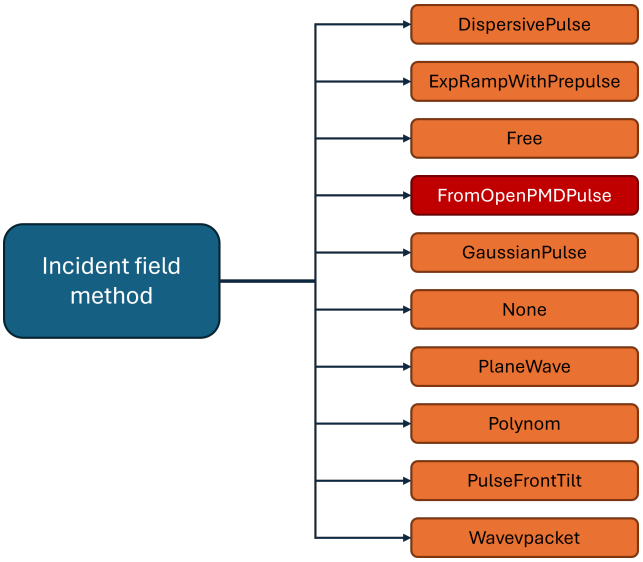

Figure 4.4: Incident field profile choices in PIConGPU. The `FromOpenPMDPulse` profile has been developed in the scope of this master thesis.

For each generating surface, an incident profile can be set, where the various options provided in PIConGPU are listed in figure 4.4). This allows incident field to enter the simulation volume coming from any direction.

4.3 The FromOpenPMDPulse profile

To read an INSIGHT measurement into a PIConGPU simulation, that has been prepared in advance according to to chapter 3.2, the `FromOpenPMDPulse` profile has been developed. It operates as incident field method, and its schematic working principle is shown in the flowchart 4.5.

In contrast to the other, already existing PIConGPU laser profiles, which calculate the incident electric laser field analytically, the `FromOpenPMDPulse` profile interpolates the experimentally measured field onto the Huygens surface.

For that, the GPUs, carrying the simulation main load, require access to the field data. Hence, the complete data set, including information about the transverse scales and time step length, must be made available to these. For this purpose, the structure `struct OpenPMDdata` has been developed, whose constructor initializes a `HostDeviceBuffer` of the size of the field chunk, fills it with the field data on the host (= CPU) side and pushes it to the device (= GPU) side afterwards. The same procedure is applied to the scales and the extent of the measurement. Before pushing the data, it undergoes certain pre-processing steps, such as

- a conversion of field values and scales into PIConGPU-internal units,
- an alignment of the field according to the selected propagation and polarisation

direction, which can be chosen independently from the INSIGHT measurement and

- a check whether the transverse simulation window extent is greater than the transverse extent of the input and, in the contrary case, an output of a respective warning stating that data from the input will be discarded.

In PIConGPU, the electric field functor constructors of incident fields are called every time step. Because of this, a simple call of `OpenPMDdata` in the constructor of `FromOpenPMDPulseFunctorIncidenE` would cause unnecessary data shifting. It is sufficient to initialize the field data and thus execute `OpenPMDdata` just once before the simulation start, as indicated in the "initialize field data block" of the flowchart 4.5, which is achieved by implementing it as a singleton. Therefore, the instance of `OpenPMDdata` in the electric field functor constructor is defined as static, so that it is generated just once and therefore the data transfer from CPU to GPU happens exclusively during the very first call of the laser profile constructor at time step 0.

To ensure the availability of sufficient free space to store the field data at the GPUs, the reserved GPU memory in `memory.param` has to be increased. Actually, this prerequisite should be considered as workaround, since it would not be necessary if the field memory allocation took place before the quite extensive particle memory allocation. Unfortunately, the electric field functor constructor, to which field memory allocation is coupled, is called only after particle memory allocation. To replace this workaround, there is need for a PIConGPU rework - e.g. by calling the laser profile once before particle memory allocation.

Especially for big field chunks with a fine resolution, memory occupancy could become a problem, as it decreases the memory available for calculations. This problem can be solved by pushing only those time slices of the input field data to the GPUs, which are necessary for the current interpolation process. However, this time-consuming procedure of pushing data slices to the GPUs has to be repeated for every time step, and not just at the beginning of the simulation, which is why this solution is supposed to be more efficient only for sufficiently big field chunks. If it will be implemented in a future refactoring, it should be coupled to the "sweet spot" in input field data size, after which it will bring performance benefits.

The pulse propagation and polarisation direction are user parameters, which can be chosen independently from the INSIGHT measurement. Currently, these are constrained along the cell edges, because the INSIGHT measurement was carried out in a plane perpendicular to the laser polarisation and propagation direction. Hence, in PIConGPU, the propagation direction must also be perpendicular to the axis-aligned Huygens surface (i.e. also axis-aligned). The structure `FromOpenPMDPulseUnitless` makes the user parameters available to the pulse profile functor and checks whether the chosen propagation and polarisation directions fulfill these requirements.

Oblique propagation can be enabled by modifying the input data. For INSIGHT measurements, small deviations from $\theta = 0°$ can be achieved easily by shifting the reconstructed near field distribution out of the center or add a linear tilt to the phase

in the far field, respectively (see chap. 3.2.7). However, this method is not applicable for greater deviations from $\theta = 0°$, e.g. for oblique propagation, which would simplify the simulation of oblique incident laser foil interaction. For that, the INSIGHT measurement has to be propagated onto an oblique, Huygens surface-aligned virtual measurement plane, or even an rectangularly bent measurement plane, if the pulse shall enter the simulation volume through a corner, as an additional step during the preparation routine. This method requires an additional refactoring of the `FromOpenPMDPulse` profile. Currently, the incident field is always centered transversely at the generating surface, as this is the usual procedure for propagation along the cell edges. Therefore, the focus position coordinate parameters, which are user-defined in other laser profiles in PIConGPU, have been discarded in the current implementation of the `FromOpenPMDPulse` profile. For oblique propagation, it would be useful to also be able to set the transverse focal coordinates (the longitudinal focus position can be set during the propagation routine, see chapter 3.2.2).

Also, oblique or circular polarisation can be implemented in a future refactoring of the `FromOpenPMDPulse` profile, but up to now there was no necessity for it, as the DRACO laser is linearly polarized, perpendicularly to the propagation direction and in the measurement plane.

After the call of `OpenPMDdata`, the simulation can start.
The core of the `FromOpenPMDPulse` profile is the function `linInterpol`, a linear interpolation routine, which extracts the transverse field slices from the data set corresponding to the current simulation time step and interpolates the field linearly onto the grid near the Huygens surface. Extrapolation is performed to $E = 0$, if necessary. The interpolated electric field is then assigned to the chosen polarisation direction. From there, the magnetic field is calculated with SVEA using the `ApproximateIncidentB` method ($\boldsymbol{B} \approx \boldsymbol{k} \times \boldsymbol{E}$), as indicated in the right part of the flowchart 4.5, and the Maxwell solver calculates the missing field components. Thus, the pulse propagates consecutively into the simulation volume.

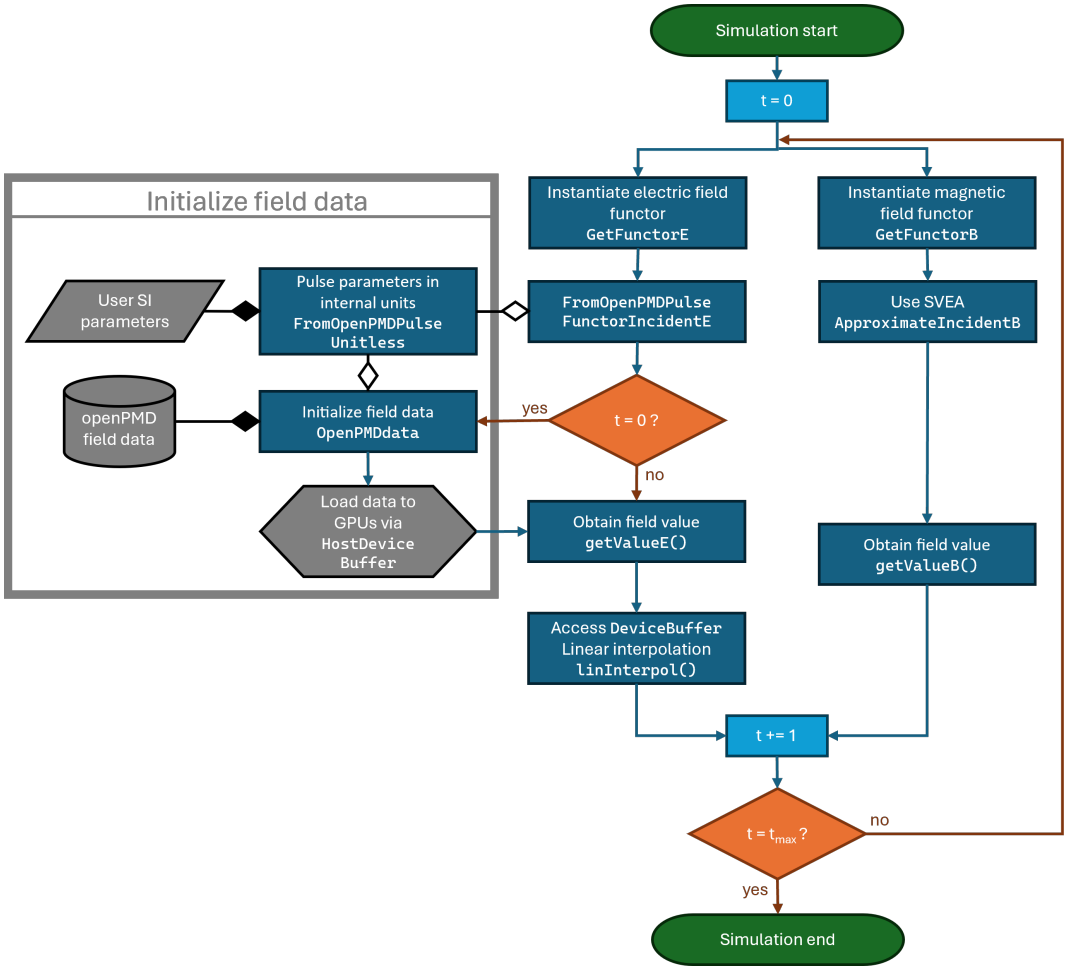

Figure 4.5: Flowchart of a PIConGPU simulation using the `FromOpenPMDPulse` profile.

4.4 Validating the FromOpenPMDPulse profile

4.4.1 Validating with Gaussian pulses in vacuum

To confirm the correct behaviour of the newly implemented `FromOpenPMDPulse` profile, it was fed with a Gaussian pulse input and compared to the `GaussianPulse` profile, that already exists in the PIConGPU repository. The underlying analytical formula (2.28) was used to write a Gaussian pulse to openPMD with the same parameters as utilized in the `GaussianPulse`, where it served as input for the `FromOpenPMDPulse` profile:

- $w_0 = 18$ µm
- $\lambda_0 = 800$ nm
- $E_0 = 9.95 \cdot 10^{12}$ V/m ($a_0 = 2.5$)
- $\tau = 13$ fs
- Propagation direction: y
- Polarisation direction: x, linear

The simulations were carried out on the high performance computing (HPC) cluster "Hemera" at HZDR on a grid with a spacing of $(1.0 \times 0.08 \times 1.0)$ µm and a time step of 2.6 fs, fulfilling condition (4.2) for the Yee field solver to operate with minimum dispersion. The Boris particle pusher was used in combination with the Ezirkepov current deposition scheme.

For all time steps during one pulse duration, the electric field in the simulation was read out at a single transverse slice shortly after the generating Huygens surface. There, the laser focus has been positioned in both simulations. Although being recorded at the same place and time in the simulation volume, those simulation outputs are not directly comparable to each other, since the electric field varies fast along the longitudinal direction with its wavelength. Thus, smallest time or longitudinal position shifts already lead to differences in the field output. These are caused by the less exact method of interpolating an external field input onto the grid near the Huygens surface and by the input being defined only at one unique longitudinal position, which may not correspond exactly to the position of the Huygens surface. In contrast to that, calculating the incident field analytically resolves the incident field exactly at the grid nodes. To bypass this problem, the output was transformed into the spectral domain with a one-dimensional Fourier transform with respect to time (2.6). Now, the results fit well to each other, as it is shown in figure 4.6. Differences only start to appear at small intensity values, about 12 orders of magnitude below the maximum intensity, and are therefore assumed to be caused by numerical precision and rounding errors.

The temporal envelope can be restored by transforming back to the time domain with (2.7). Again, both pulses fit well, shown in figure 4.7, apart from differences due to numerical precision at small amplitude values.

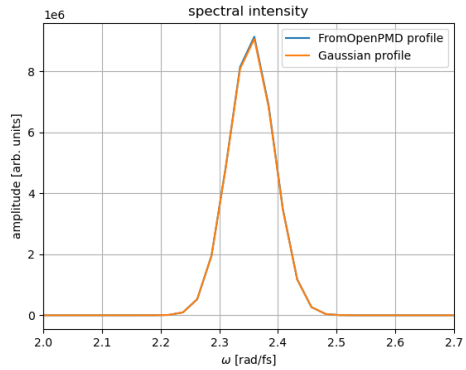

(a) Spectral intensity, transversely integrated.

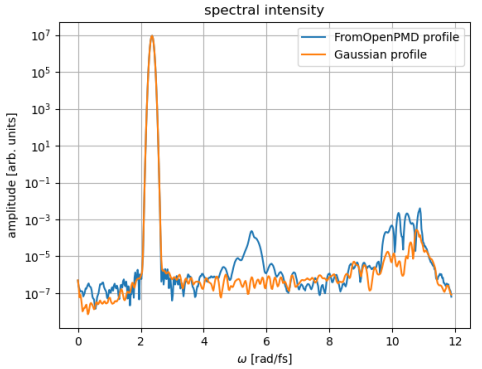

(b) 4.6a on a logarithmic scale.

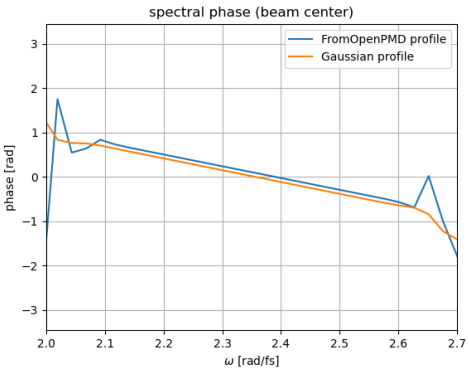

(c) Spectral phase along the pulse center. The phase offset between the two pulses is irrelevant, since it is global.

Figure 4.6: Comparing a Gaussian pulse in the spectral domain, obtained with the `GaussianPulse` and the `FromOpenPMDPulse` profiles. Apart from differences at small amplitude values, assumed to be caused by numerical precision, the results fit well.

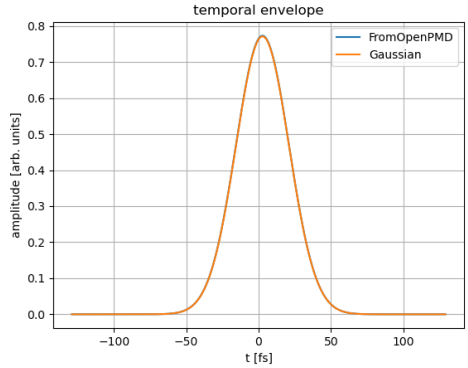

(a) Temporal envelope along the pulse center.

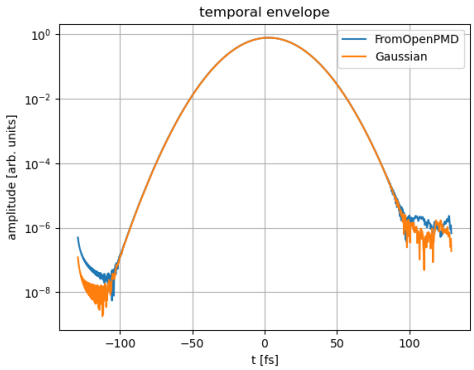

(b) 4.7a on a logarithmic scale.

Figure 4.7: Comparing the temporal envelope of a Gaussian pulse, obtained with the `GaussianPulse` and the `FromOpenPMDPulse` profiles. Apart from differences at small amplitude values, assumed to be caused by numerical precision, the results fit well.

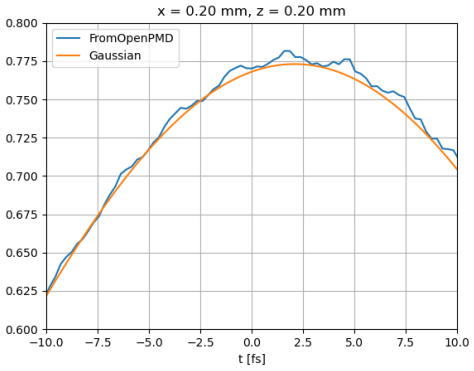

Figure 4.8: The effects of a time sampling of the input field in openPMD differing from the simulation time steps. The relative amplitude deviation is about 1%.

Furthermore, the impact of the linear interpolation routine was investigated. This especially affects the temporal axis, due to the fast field oscillation. In the simulations, the time step was chosen to be $\Delta t = 2\pi/(10\omega_0)$, which means that in the worst case of the input field being sampled at times exactly between the actual simulation time steps, the linear interpolation can cause deviations of up to $\Delta E = 1 - \cos(\omega_0 \Delta t/2) = 5$ % from the actual field value. In the case of the Gaussian pulse considered here, a time sampling of the input field deviating from the simulation time steps results in a "wiggly" temporal envelope, which is shown in figure 4.8, even though the deviation in Δt was limited to a few percent. Due to the temporal axis of the input comprising $\sim 10^3$ samples, the deviation will accumulate as the simulation time progresses. Since relevant laser-plasma interaction takes place in the highly nonlinear regime, it is very sensitive to such small deviations in the field of the laser pulse (see chap. 5.1). Hence, these should be avoided by adjusting the time sampling of the input field according to the simulation time step (see chap. 3.2.3).

The effect of the linear interpolation routine on the transverse directions is less severe, since there the field typically does not vary as strongly. However, as the spatial resolution of the INSIGHT measurement device is limited, the transverse sampling of INSIGHT measurements can be coarser than the transverse grid of PIC simulations. For example, the presented INSIGHT measurement has about 5 sample points per w_0, but typical PIC-simulations require a transverse grid resolution of $\Delta x \gtrsim w_0/10$ to ensure that the field gradient between adjacent grid nodes remains sufficiently small, thereby ensuring the accuracy and reliability of the results. If this deviation becomes too big, a transverse sampling adjustment of an INSIGHT measurement may be necessary, which is done preferably by Fourier interpolation, i.e. padding zeros around the reconstructed near field before transforming back with (2.21), as this routine provides a higher order accuracy than linear interpolation.

Another approach than the grid adjustment can be the implementation of a higher order interpolation routine instead of linear in the `FromOpenPMDPulse` profile in a future refactoring.

4.4.2 Validating with INSIGHT measurements in vacuum

To confirm the correct pulse propagation behaviour during the simulation, the example INSIGHT measurement was propagated to $-z_R$ (chap. 3.2.2) before reading it into the simulation with the `FromOpenPMDPulse` profile and then propagating it to the focus position in the simulation. There, the simulation output was compared to the original INSIGHT measurement (i.e. in the focal plane). As it can be seen in figure 4.9, these match well, in terms of pulse extent, amplitude and substructure (e.g. halos, pre- and post-pulses).

To compare the longitudinal axes, the approximation

$$z \approx -ct \tag{4.3}$$

has been used, which holds for short pulses ($z_R \gg c\tau$). This applies to the INSIGHT pulse, since $c\tau/z_R = 6 \cdot 10^{-3} \ll 1$, which is why the deviation caused by this approximation should be negligibly small. Hence, small differences, such as the missing double-peak structure at the pulse maximum in figure 4.9b, are assumed to be caused mainly by field solver dispersion, since the Yee field solver was used with a rather coarse longitudinal sampling of $\Delta y = \lambda/10$ and axis-aligned propagation along the y-axis over a long distance of $z_R = 1.6 \cdot 10^4 \Delta y$.

Additionally, the pulse energy conservation and the validity of the approximations in the energy calculation (chap. 3.2.4) were verified. Thereto, the energy density

$$W = \iint \frac{\varepsilon_0}{2}(\boldsymbol{E}^2 + c \cdot \boldsymbol{B}^2)\ dx\ dy$$

has been calculated for both simulation output and INSIGHT measurement. For the latter, the approximations outlined in chapter 3.2.4 were applied to solve the integral. In contrast to that, no field components were neglected for the calculation of the energy density of the simulation output, but it is still lower than the input energy density, as it can be obtained in figure 4.9c. This trend continues in the total pulse energy, where the output pulse energy (calculated with (3.1)) lies about 8% below the input value (calculated with (3.5)). This effect can be attributed to discretisation errors, caused by a coarse (especially longitudinal) sampling of $\lambda/10$, which truncates the amplitude of the fields involved (see fig. 4.10). Improvement can be achieved with a smaller longitudinal sampling: for $\lambda/20$, the output energy lay only 4% below the input value.

Furthermore, test-runs for different propagation and polarisation directions were conducted. Again, the field was read out shortly after the generating Huygens surface and compared to the input. From figure 4.11 it can be obtained, that the fields rotate as expected to fulfill the user input parameters while keeping the system handiness.

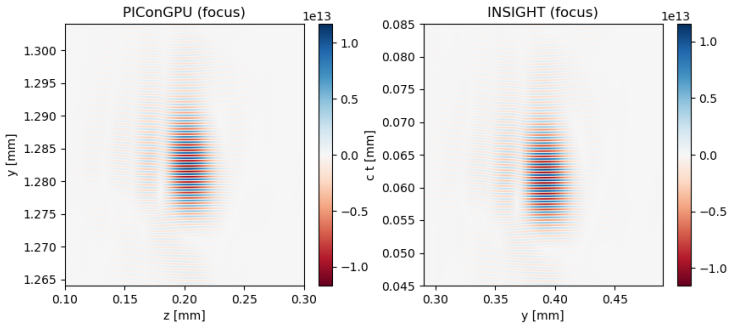

(a) Comparing the pulse central slices.

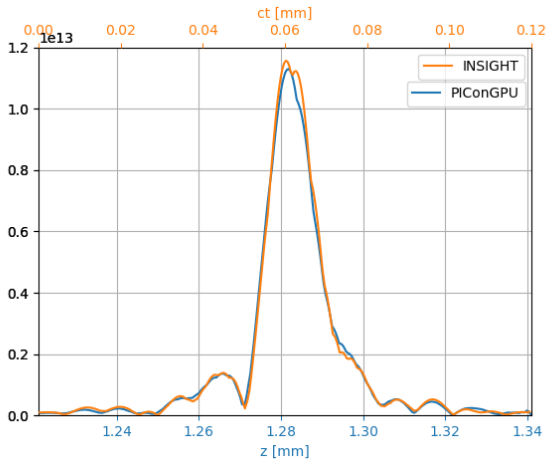

(b) Comparing the longitudinal envelope along the pulse center.

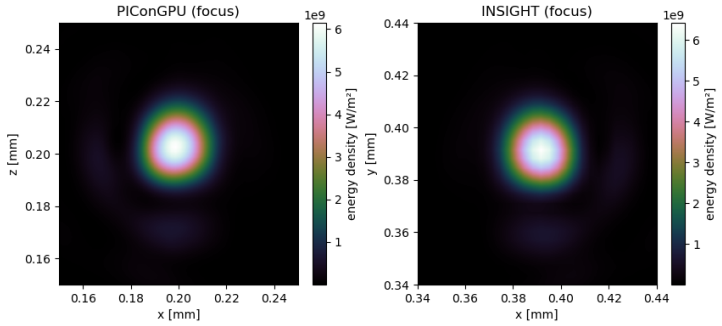

(c) Comparing transverse extent and energy density. The simulation output appears transposed due to a changed propagation and polarisation direction.

Figure 4.9: Comparing simulation output to the INSIGHT measurement. Please note that the propagation axis has been changed from z (INSIGHT) to y (PIConGPU) and the polarisation axis from y to x, and that the longitudinal axis of the INSIGHT measurement is approximated with (4.3).

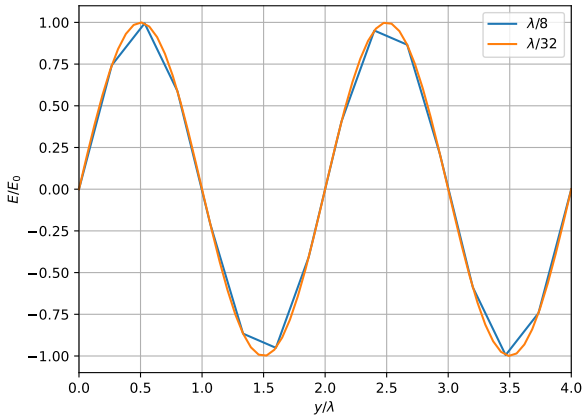

Figure 4.10: An oscillating electric field, differently sampled. A coarse sampling can truncate the amplitude and thus cause energy loss.

Additional tests were carried out for asymmetric input field chunks as well as asymmetric simulation cells, where the results did not differ from the symmetric case. Also, the number of GPUs involved in the simulation has no effect on the simulated laser field.

Given that all validation tests were conducted successfully, it can be concluded that the `FromOpenPMDPulse` profile functions as expected.

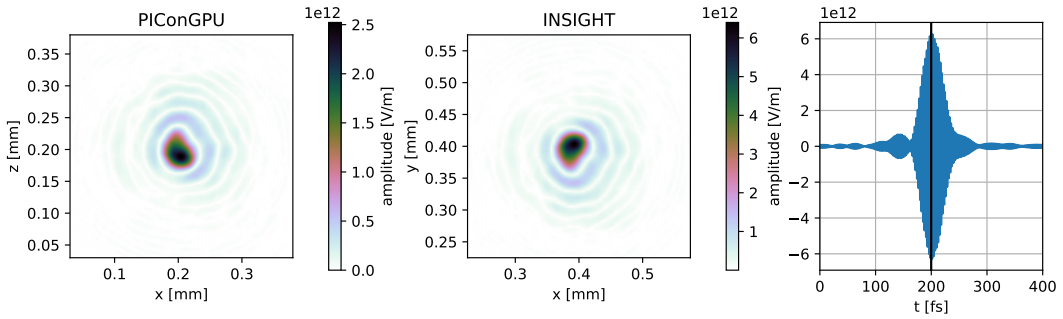

(a) A propagation direction change $z \to +y$ while keeping $+x$ as polarisation direction leads to an inverted transverse axis $y \to -z$ to maintain the system handiness.

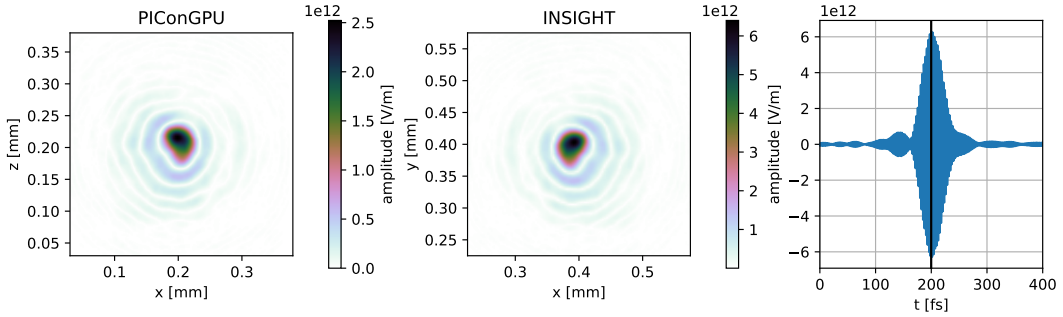

(b) Additionally inverting the polarisation direction $x \to -x$ does not invert the second transverse axis $y \to +z$.

Figure 4.11: Effects of a coordinate system rotation. Left: simulation output, electric field close to the Huygens surface. Center: electric field slice of the simulation input (INSIGHT measurement) at the same time and position as the simulation output. Right: temporal evolution of the pulse center, where the black vertical line marks the corresponding simulation time step. If propagation and polarisation direction in the simulation differ from the input, the field will be rotated such that the user input parameters are fulfilled while keeping the system handiness. Due to the fast oscillation of the field along the temporal axis, it is sensitive to small temporal shifts introduced by a different temporal sampling of simulation input and output, which is why the amplitudes differ.

5 Application of the INSIGHT measurement to laser-plasma simulations

5.1 Laser-Wakefield acceleration

The principle of Laser-Wakefield acceleration (LWFA) has first been presented in 1979 [39] and relies on the excitation of wake plasma-waves by ultrashort laser pulses propagating through an underdense plasma ($\omega_0 > \omega_P$, where $\omega_P = \sqrt{ne^2/(m\varepsilon_0)}$ is the plasma frequency). The ponderomotive force of the pulse causes a displacement of the plasma electrons relative to the heavier background ions, which are assumed to remain approximately static. Once the pulse has passed, the ions draw back the electrons, thereby creating a plasma oscillation propagating behind the pulse, where electrons can be trapped and subsequently accelerated by the charge separation field. There, accelerating field gradients of up to several hundred GV/m [40] can be achieved, which exceed common linear accelerators by far. Hence, electrons "riding" the plasma wake can be accelerated to relativistic energies over remarkably short distances, grouped into extremely short bunches in the sub-picosecond range [40].

The evolution of plasma wakes is highly dependent on the pulse intensity [40]. In the linear regime ($a_0 \ll 1$), the plasma wave is a simple sinusoidal oscillation with frequency ω_P and the energy of the accelerated electrons follows an exponential decaying distribution.

In the nonlinear (relativistic) regime ($a_0 \gtrsim 1$), where LWFAs usually operate, the plasma wave steepens and its period lengthens [40]. The ponderomotive force of the laser can be strong enough to expel all background electrons from the first wake [41], thereby creating a co-propagating ion cavity (*blow-out regime*, shown in figure 5.1). Electrons, that are injected into the cavity, are accelerated by the longitudinal electric field of the plasma wave to relativistic energies. In difference to the linear regime, the energy spectrum of these electrons is plateau-like or even sharply peaked.

5.2 Self-truncated ionization injection

There exist many mechanisms to inject electrons into the cavity, where the simplest would be self-injection of background electrons, that can result from laser-plasma instabilities due to the coupling of Raman side- and backscatter to the wakefield [40]. As self-injection occurs uncontrolled, only at high laser intensities and typically

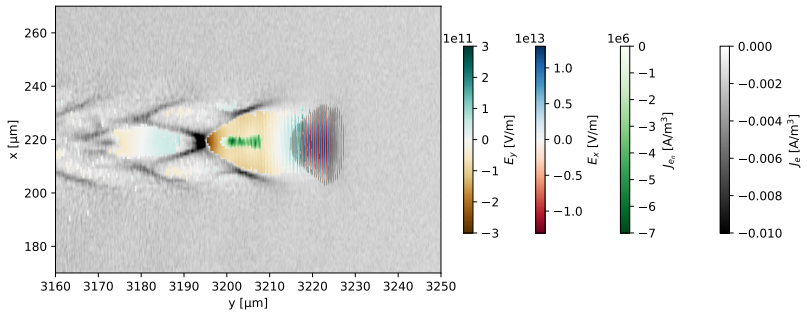

Figure 5.1: Laser-plasma interaction in the blowout regime. The current density of the background electrons is depicted in gray, and the electrons injected by STII into the evacuated cavity, experiencing the accelerating longitudinal field $E_y < 0$, in green.

results in a large energy spread of the accelerated electrons, it is not the preferred injection method for the creation of reproducible acceleration conditions.

Better control over the injection process provides, for example, ionization induced injection, that relies on the increased K-shell ionization threshold of high-Z gas atoms [14, 42]. Therefore, the low-Z gas (H or He) in the gas target is doped with a high-Z gas (e.g. N), usually with a small fraction of $\lesssim 1$ %. The K-shell electrons are then only ionized near the laser intensity maximum at the front of the cavity, thereby enabling their injection. Continuous electron injection and thus a broad energy bandwidth can be avoided by a self-truncation of the process due to the evolution of laser and cavity (*self-truncated ionization injection*, STII [42]), which constrains the injection process to a region of typically ~ 100 µm along the laser propagation distance in the target. Self-truncation is caused by the relativistic self-focusing of the laser, which mainly drives the laser evolution in the plasma if the laser power exceeds the critical power [43]

$$P_C\ [\mathrm{GW}] \approx 17 \left(\frac{\omega_0}{\omega_P}\right)^2 .$$

By placing the laser focus a few millimeters behind the start of the target, laser-plasma interaction already starts in the mid field of the laser with a relatively big spot size, which will evolve significantly after entering the plasma, as relativistic self-focusing enhances the original focusing of the laser pulse. As the intensity of the focused pulse increases, the ionization position shifts forwards, relative to the pulse maximum. Thus, the freshly ionized electrons are exposed to the decelerating fields, which dominate the first half of the cavity, over a longer distance. Therefore, the electrons become too slow for being trapped in the cavity, which is why injection terminates.

With this injection mechanism, high-quality electron beams with quasi-monoenergetic spectra can be produced.

5.3 Influence of a mask in the laser beamline onto a LWFA setup

5.3.1 Simulation setup

As a first application of the `FromOpenPMDPulse` profile, the influence of a mask placed in the laser beamline onto LWFA-accelerated electrons shall be investigated.

Therefore, a 3D LWFA simulation has been set up in PIConGPU, whereby [44] was used as reference. As laser profile, the previously discussed example INSIGHT measurement was selected, with a pulse energy of 3 J ($a_0 = 2.4$). The laser focus was positioned at $y_f = 1.2$ mm, propagating into positive y direction and polarised linearly along the x axis. The simulation was carried out once with the original INSIGHT measurement as input, and then repeated after applying a mask of a diameter of 38.5 mm positioned at a distance of 1 m in front of the focus to the pulse. The effects of this mask onto the laser focal spot have already been discussed in chapter 3.2.6, and now the effects onto the accelerated electrons is of interest.

The simulation results of both realistic pulses were compared to those using a similar Gaussian pulse profile ($a_0 = 2.4,\ w_0 = 18$ µm$, \lambda_0 = 800$ nm, $\tau = 26$ fs), with the aim of investigating the impact of the STCs in the INSIGHT pulse on the properties of accelerated electrons.

The gas density profile, used throughout all simulations, is plotted in figure 5.2. It follows a flat-top distribution with an electron density of $n_0 = 3.3 \cdot 10^{24}$ m^{-3} between $y_{\text{start}} = 1.1$ mm and $y_{\text{end}} = 3.0$ mm. At the edges, the gas density falls off following a Gaussian distribution with $\sigma = 0.26$ mm, starting from zero before y_{start} and ending in a plateau of $n = 0.012\ n_0$ after y_{end}. The plasma consists of pre-ionized helium He^{2+} at $T = 0$ K, of which only the free electrons have been included into the simulation, because the ions are assumed to be static at simulation time scales. The pre-ionization is assumed to be the effect of a pre-ramp of the laser pulse, which is not included in simulation because it typically extends over a range of various picoseconds and would thus go beyond the scope of PIC simulations. To enable STII as injection method, the gas is doped with 3 % nitrogen, which is also pre-ionized to N^{5+}, so that only the K-shell electrons remain bound.

The simulation window had an extent of $(416 \times 133 \times 416)$ µm and a cell size of $(1.0 \times 0.05 \times 1.0)$ µm and moved along the y axis with c, following the laser pulse. The simulation time step was chosen to be

$$\Delta t = \frac{0.995}{c\sqrt{\frac{1}{\Delta x^2} + \frac{1}{\Delta y^2} + \frac{1}{\Delta z^2}}} = 0.17 \text{ fs},$$

since this choice minimizes field solver dispersion by fulfilling (4.2). The macroparticles were initialized randomly distributed with an average density of one macroparticle per cell. The particle shape was chosen to be represented by a piecewise cubic spline. The Yee field solver was used in combination with the Boris particle pusher and the Ezirkepov current deposition scheme.

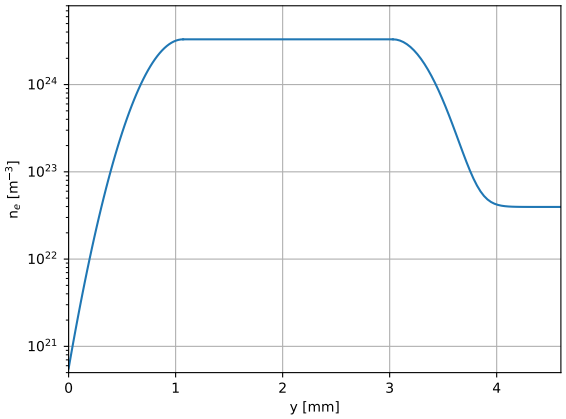

Figure 5.2: Gas profile of the STII LWFA setup.

5.3.2 Results

The development of the energy distribution of the ionization-injected nitrogen electrons over time is plotted in figure 5.3. In all simulations, injection starts at $t \approx 4$ ps. At this time, the waist size of the plasma self-focused, masked INSIGHT pulse is about 0.4 µm smaller than the unmasked one (see fig. 5.4), although in vacuum the focal spot would be slightly bigger (chap. 3.2.6). Also, the transverse extent of the ionization area and thus the transverse extent of the injected electron bunch decreases by a factor ≈ 0.7 under the influence of a mask, which can be concluded from a comparison between figures 5.5a and 5.5b. The electron bunch interacts with the INSIGHT pulse, which can be concluded from the longitudinal oscillation of the electron density with the pulse central wavelength λ_0.

Figures 5.6a and 5.6b show that the amplitude of the longitudinal (accelerating) field remains the same, which is why the injected electrons acquire energy with a similar rate until $t = 11.5$ ps, where the pulse begins to exit the plasma and the acceleration process stops (fig. 5.3).

At the same time, abundant down-ramp injection of background electrons takes place, starting from the back of the cavity, as it can bee seen in figure 5.7. The energy histogram of the background electrons (fig. 5.8) reveals, that these reach only low energies. As the plasma density decreases, the cavity elongates rapidly and thus also the longitudinal extent of the decelerating field $E_y > 0$, which dominates its front area. For $t \gtrapprox 13$ ps, the cavity becomes too long to fit into the simulation window (see fig. 5.9), which is why the injected background electrons start to slip out of the simulation volume, together with the accelerating rear part of the cavity ($E_y < 0$). This leads to the energy decay in the background electron histogram for $t \gtrapprox 13$ ps. The STII nitrogen electron bunch still travels closely behind the laser pulse (see fig. 5.9) and is thus unaffected by parts of the cavity leaving the simulation volume.

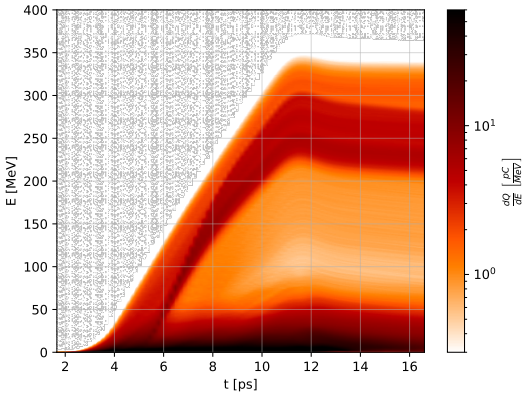

(a) INSIGHT, without mask.

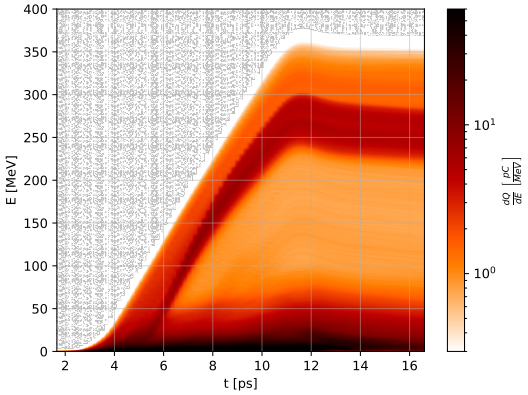

(b) INSIGHT, with mask.

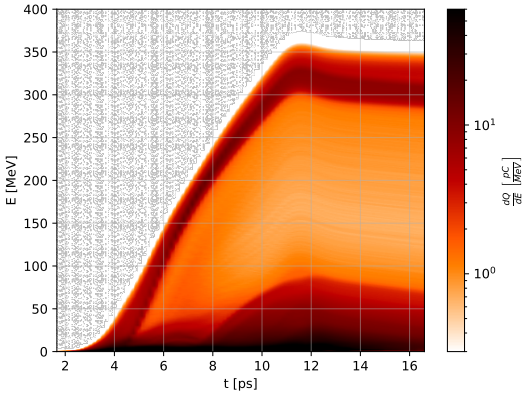

(c) Gaussian pulse profile.

Figure 5.3: Energy distribution of the injected nitrogen electrons over time for different pulse profiles.

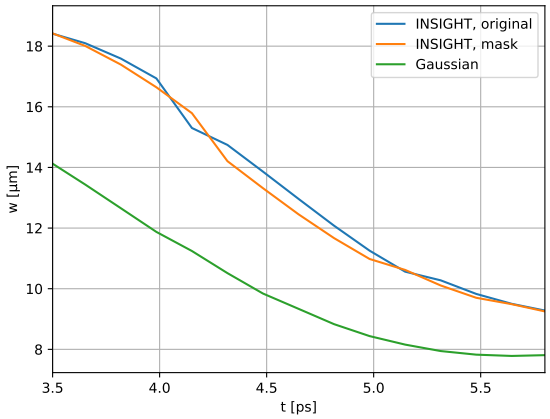

Figure 5.4: Development of the laser waist size over time (plasma self-focusing) for different laser profiles.

The properties of the accelerated nitrogen electrons can be extracted from the electron spectrometers, which relate the energy distribution of the electrons to their directional divergence. For $t = 11.6$ ps, these are shown in figures 5.10a and 5.10b. From there, the mean electron energy E_{mean} and the energy spread ΔE and their respective uncertainties were extracted with a supergaussian fit of power two using the scipy `curve_fit` routine, and the electron divergence θ and their directional offset θ_{offset} with an ordinary Gaussian fit. The charge has been calculated by integrating over the bunch in the electron spectrometer. The electron bunch length has been obtained from the longitudinal phase space plots (figs. 5.11a, 5.11b), where the uncertainty represents the width of a bin along the y axis. All those parameters are listed in table 5.1.

	without mask	with mask	difference
E_{mean} [MeV]	265(3)	271.1(18)	+2 %
E_{max} [MeV]	369	377	+2 %
ΔE_{FWHM} [MeV]	93(13)	66(9)	−41 %
θ_{offset} [mrad]	−4.265(7)	−2.029(7)	−52 %
θ_{FWHM} [mrad]	27.585(23)	24.586(23)	−10 %
Q [pC]	190(6)	144(5)	−24%
Δy_{FWHM} [µm]	4.90(16)	4.55(16)	(-8 ± 4) %

Table 5.1: Comparing LWFA electron properties at $t = 11.6$ ps in dependence of a mask.

Additionally, the spectrometers reveal a grouping of the electrons into two aggregations of slightly different energies ($\Delta E \approx 25$ MeV), where the higher-energy aggregation exhibits a smaller divergence. The longitudinal phase-space (figs. 5.11a,

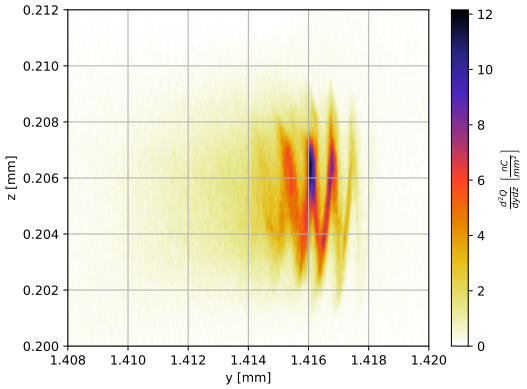

(a) Original INSIGHT pulse profile.

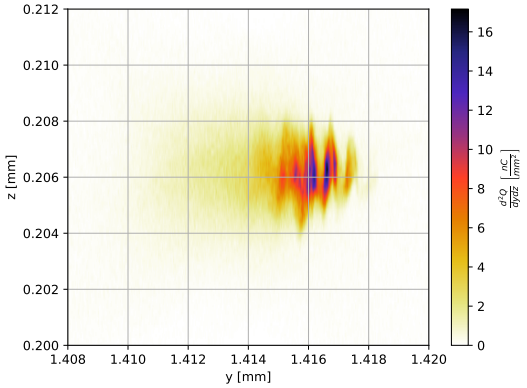

(b) INSIGHT with applied mask.

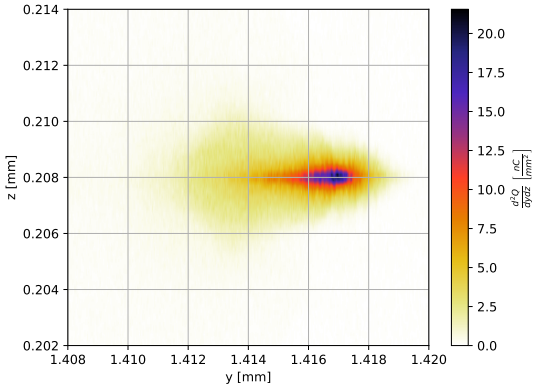

(c) Gaussian pulse profile.

Figure 5.5: Extent of the nitrogen electron bunch at $t = 5.0$ ps for different pulse profiles.

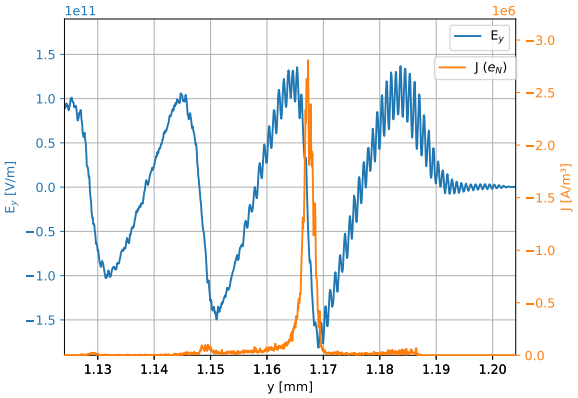

(a) Original INSIGHT pulse profile.

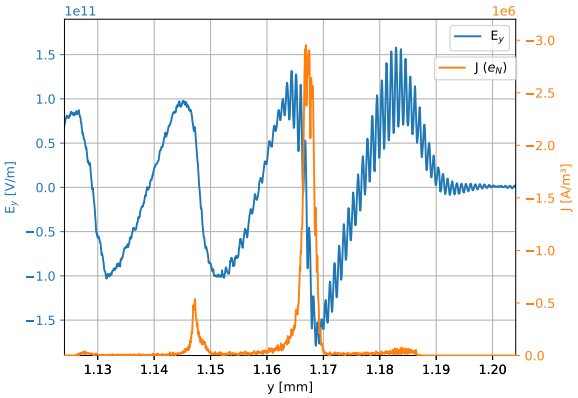

(b) INSIGHT with applied mask.

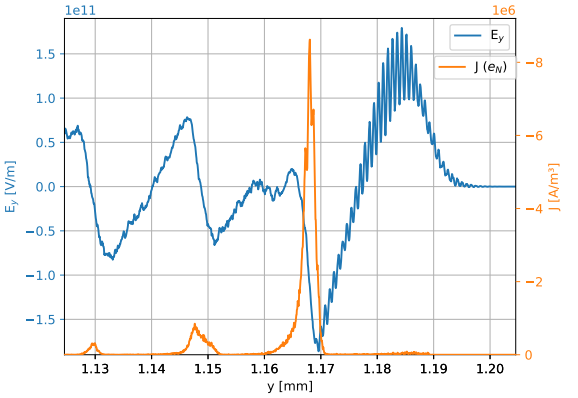

(c) Gaussian pulse profile. The second maximum of E_y is distorted due to the presence of the more efficiently injected electrons (please note the different J scale).

Figure 5.6: Longitudinal field E_y and current density J of freshly injected nitrogen electrons at $t = 4.1$ ps for different pulse profiles. E_y is superimposed by oscillations of the central pulse wavelength.

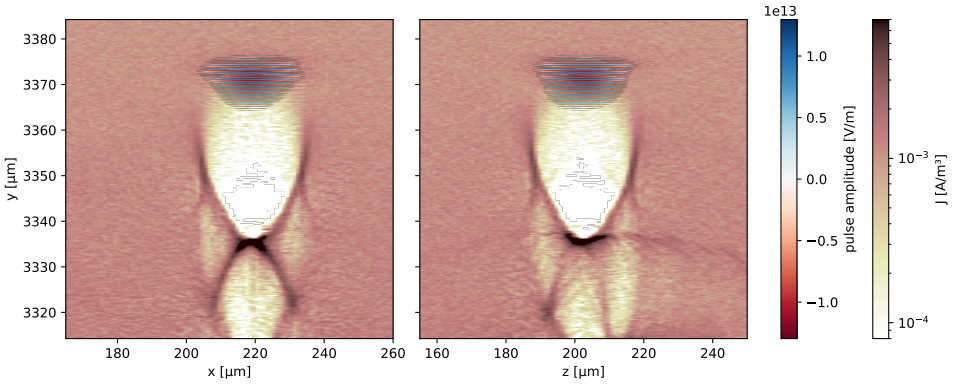

(a) $t = 11.46$ ps

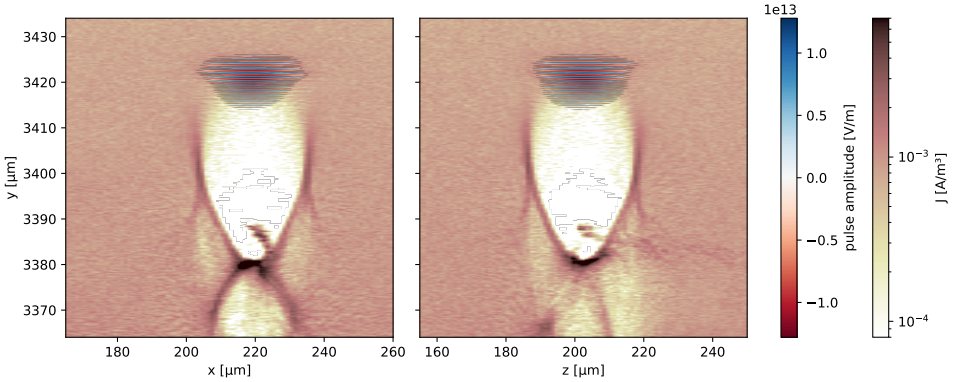

(b) $t = 11.62$ ps

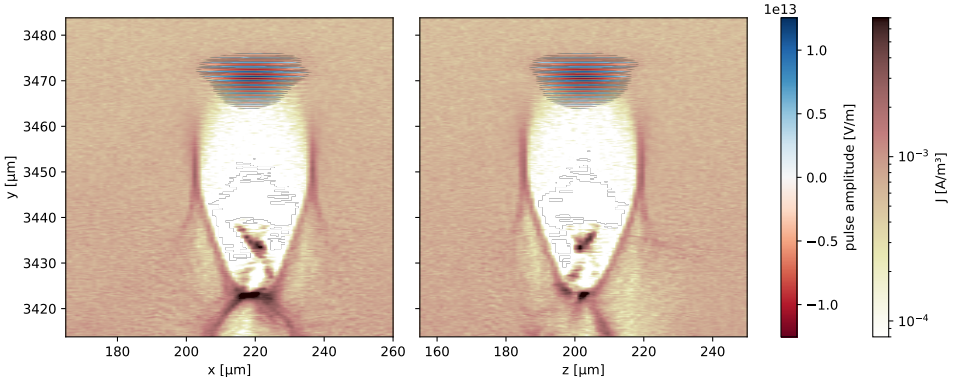

(c) $t = 11.79$ ps

Figure 5.7: Down-ramp injection of background electrons from the back of the cavity for $t \gtrapprox 11.5$ ps, where the pulse begins to exit the plasma. The cavity deforms and starts elongating. The STII nitrogen electrons are not shown. This process was witnessed throughout all simulations, but here only the results utilizing the original INSIGHT pulse profile are shown.

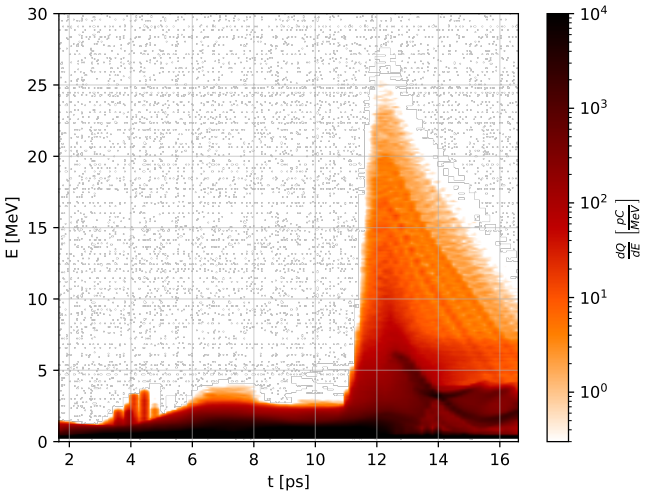

Figure 5.8: Energy histogram of the background-electrons, undergoing down-ramp injection for $t \gtrapprox 11.4$ ps, recorded using the original INSIGHT pulse profile.

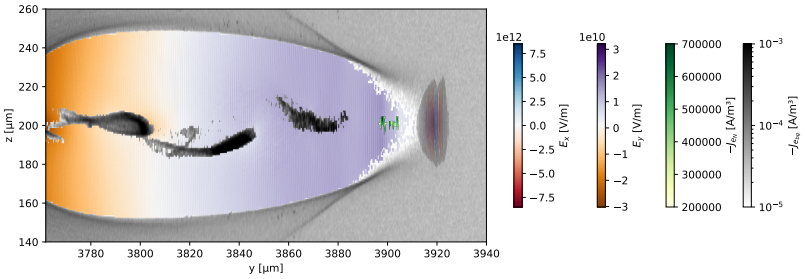

Figure 5.9: Elongated ion cavity and longitudinal field E_y of the original INSIGHT pulse profile at $t = 13.3$ ps. The STII nitrogen electron bunch (green) travels still closely behind the laser pulse, whereas the down-ramp injected background electrons (brown) are spread over the whole longitudinal extent of the cavity. Thus, these tend to leave the simulation volume through its rear end together with the accelerating (orange) part of the cavity.

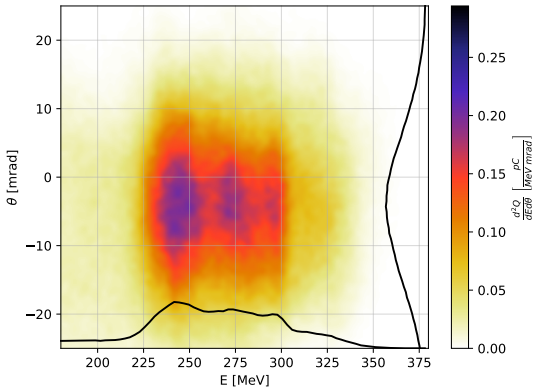

(a) Original INSIGHT pulse profile

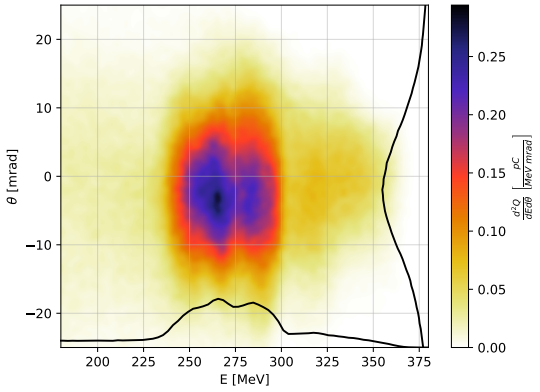

(b) INSIGHT pulse profile with mask

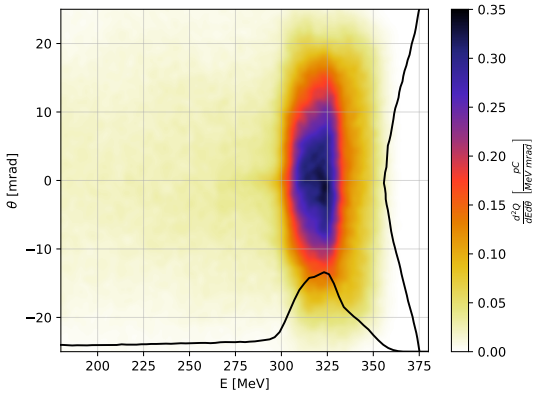

(c) Gaussian pulse profile

Figure 5.10: Nitrogen electron spectrometers at $t = 11.6$ ps for different laser profiles.

5.11b) reveals, that these are also separated in space. The few high-energy electrons ($E > 300$ MeV) precede the main bunch, followed by the electrons that form the lower-energy aggregation in the spectrometers, whereas the higher-energy electron aggregation follows last.

The Gaussian pulse profile behaves similarly to the INSIGHT pulse profiles throughout the simulations. Ionization-injection starts approximately at the same time ($t \approx 4$ fs, see fig. 5.3c), but the electron bunch is more compact, as the transverse extend is reduced by a factor of 1/6. The charge density is enhanced by a factor ≈ 1.8 and does not exhibit oscillations with λ_0 (fig. 5.5c), in contrast to the simulation using the original INSIGHT pulse profile. The decreased transverse bunch size also reflects in a smaller (self-focused) waist size compared to the INSIGHT pulses (see fig. 5.4), although the waist sizes at the start of the plasma (i.e. at $t = 0$) were ordered reversely with $w_{\mathrm{INSIGHT}} = 22$ µm and $w_{\mathrm{Gauss}} = 25$ µm (according to (2.27) with $z = y_f$).

The amplitude of the longitudinal field at the time of injection, plotted in figure 5.6c, is enhanced by a factor ≈ 1.3 and the current density of the nitrogen electrons is about 3 times higher, compared to the INSIGHT pulse profiles. The higher density of injected electrons distorts the longitudinal field as it lowers the maximum of the second plasma wave. The rate of energy acquirement is comparable to the INSIGHT pulse profiles, apart from the very first picosecond after the beginning of injection, where it is enhanced. Hence, the accelerated electrons acquired a higher energy at the end of the plasma. Furthermore, they exhibit less energy spread and no directional offset, which can be concluded from the electron parameters extracted from the respective spectrometer, shown in figure 5.10c. At $t = 11.6$ ps, the following electron parameters were extracted:

- $E_{\mathrm{mean}} = 320.6(16)$ MeV (+21 %)
- $\Delta E_{\mathrm{FWHM}} = 40(7)$ MeV (−59 %)
- $E_{\mathrm{max}} = 371$ MeV (+0.5 %)
- $\theta_{\mathrm{offset}} = 0.081(7)$ mrad (to 0.4 %)
- $\theta_{\mathrm{FWHM}} = 34.290(23)$ mrad (+24 %)
- $Q = 143(4)$ pC (−25 %)
- $\Delta y_{\mathrm{FWHM}} = 4.60(16)$ µm (-7 ± 4 %)

The parameter change refers to the simulation using the original INSIGHT pulse profile.

The longitudinal phase space (fig. 5.11c) follows a S-shaped curve, similar to the INSIGHT pulse profiles simulations, but more smoothly distributed and with a higher peaked charge density. Again, the electrons in the center of the bunch have slightly less energy (fig. 5.11c). The smaller extent of the curve along the momentum axis also reflects in a smaller energy spread in the spectrometer (fig. 5.10c).

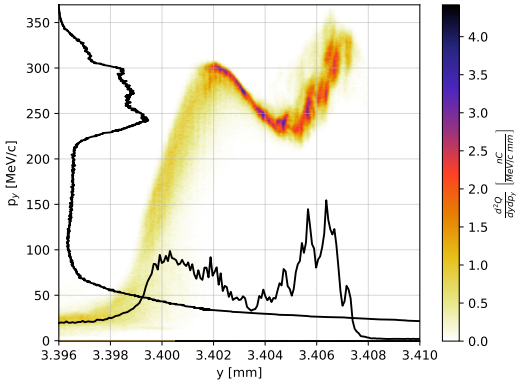

(a) Original INSIGHT pulse profile

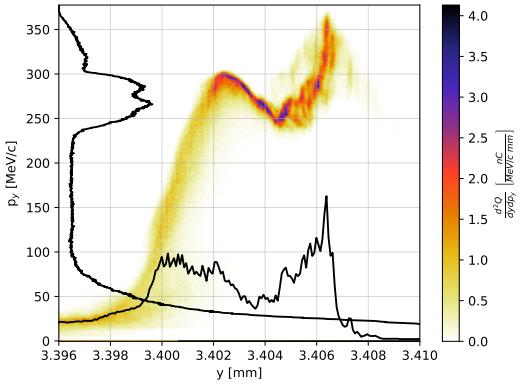

(b) Masked INSIGHT pulse profile

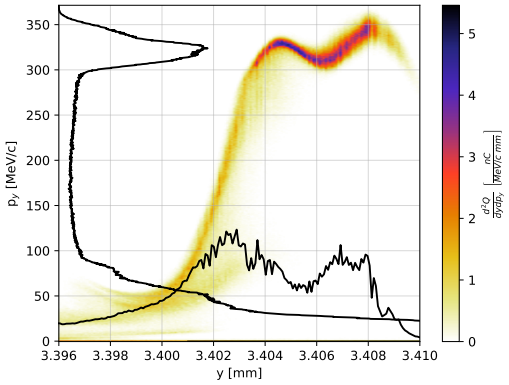

(c) Gaussian pulse profile

Figure 5.11: Longitudinal phase space of the nitrogen electrons at $t = 11.6$ ps for different pulse profiles.

There, the division of the electrons into groups of two different energies cannot be observed, instead these appear accumulated into one single, quasi-monoenergetic accumulation.

When the pulse starts exiting the plasma at $t \approx 11.5$ ps, down-ramp injection of background-electrons starts and the acceleration process of the ionization-injected nitrogen electrons stops, similar to the INSIGHT pulse profile simulations.

5.3.3 Discussion

The presented results indicate a slight improvement of the LWFA electron parameters by placing a mask in the laser beamline, in terms of a reduction of energy spread, divergence and directional offset and a modest enhancement of mean and maximum electron energy. This can be attributed to a more efficient injection process, which takes place in a smaller transverse extent and results in a more compact electron bunch. The more Gaussian-like transverse pulse shape of the masked pulse and a faster relativistic self-focusing can serve as explanation for that.

Remarkable is also the decreasing directional offset of the electrons, that has been witnessed throughout the complete simulation duration and also in re-runs, which is why it cannot be attributed to a random initial particle position. Also the directional uncertainty of the laser propagation direction $\Delta\theta = 0.5$ mrad after centering the near field (chap. 3.2.7) is too small to serve as unique explanation, although the directional precision of the laser pulse increases with a mask positioned around $(x = 0, y = 0)$, because the transverse sampling in the mid field at the mask position decreases with $\Delta x_{\mathrm{MF}} = \Delta x_{\mathrm{NF}} \cdot d/f$. Thus, the primary cause of the directional offset is likely attributable to the transverse field distribution of the laser pulse, which deviates significantly from a Gaussian profile when out of focus, at the point where the interaction with the gas begins.

Still, the improvements achieved with a mask are not sufficient to approach those LWFA electron parameters obtained with a similar, but STC-free Gaussian pulse profile. There, mean electron energy and energy spread remain unrivaled, and can be attributed to an even more efficient initial electron injection and acceleration caused by the pulse's "perfect" transverse shape and a more efficient self-focusing in plasma.

Also, the differences between the simulations with and without mask are not big enough to explain the effects of a mask witnessed in similar LWFA-STII experiments with the DRACO laser at HZDR. In a corresponding campaign in April 2024, a mask improved the electron parameters significantly for constant beam parameters and partly made injection possible at all, as it can be concluded from the electron spectrometers of consecutive shots, depicted in figure 5.12. Also, the mask seemed to improve the stability of the pulse and lowered the shot-to-shot fluctuation, which of course cannot be verified with an INSIGHT measurement due to its averaging nature. Since the pulse parameters in this very experiment differed from the pulse parameters in the above presented simulations, a comparison between the obtained spectrometers is limited to their rough appearance. For example, the two electron

aggregations differing slightly in energy, where the higher-energy aggregation exhibits a lower divergence, are visible in most spectrometers of figure 5.12b, similarly to the simulation results. These aggregations result from the slightly differing ionization energies for the two electrons in the K-shell of nitrogen, so that these are not ionized at the same time.

The differences in simulation and experiment can partly be attributed to mask-independent laser parameters differing slightly from the usual experimental STII settings, such as a focus position located behind the gas target and a lower pulse energy (≈ 2.5 J) [14].

Additionally, it is likely that the INSIGHT measurement does not precisely capture the true laser characteristics. The assumption of perfect compression may be overly simplistic, and the pulse could exhibit an unknown residual phase. Alternatively, the resolution may have been insufficient, or critical information about the pulse may have been lost during the averaging process.

Also, the realistic gas profile will deviate from the idealized simulation (fig. 5.2). Usually, a nitrogen doping concentration of $\lesssim 1$ % [14] is used, which is lower than the value used in the simulation, and the assumption of zero temperature does not accurately reflect the conditions in LWFA experiments. Furthermore, a realistic gas profile will most likely exhibit density fluctuations, a transverse position-dependent longitudinal extent and non-Gaussian edges. Analogously to a realistic laser, it may vary from shot to shot. To create a complete digital twin of the experimental setup, a precise knowledge of the gas profile will be necessary.

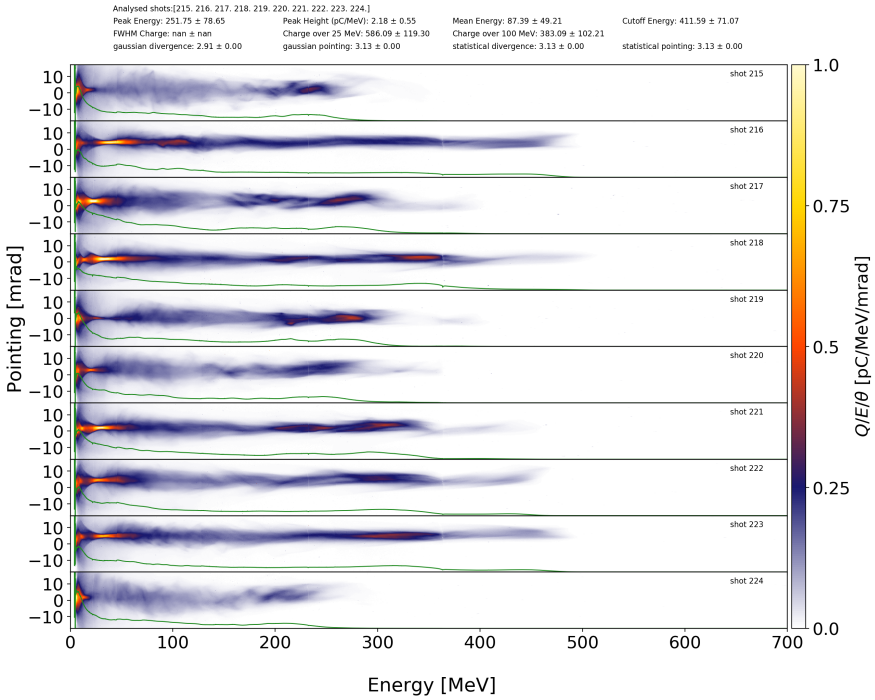

(a) without mask

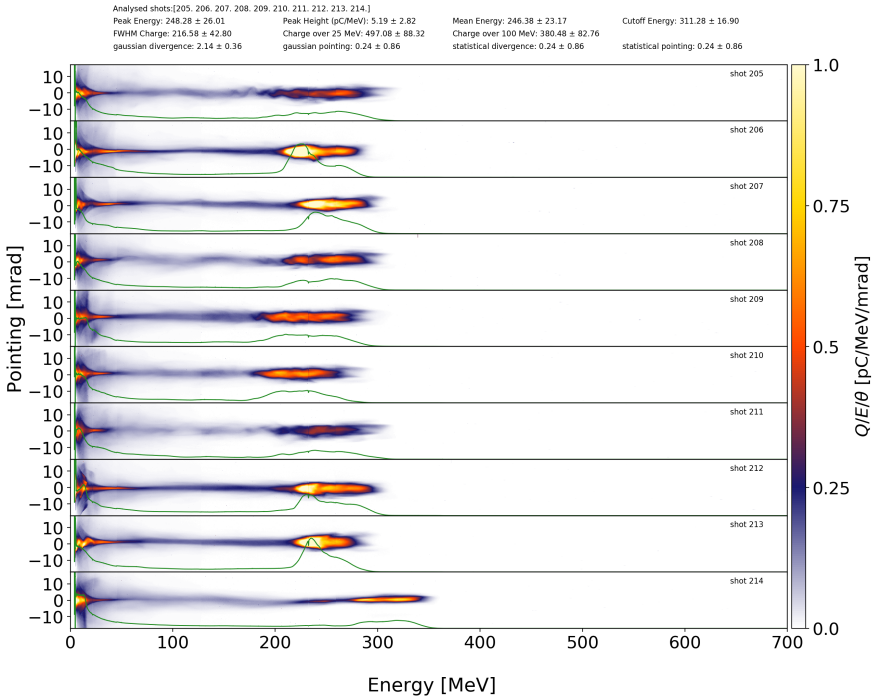

(b) with mask

Figure 5.12: Electron spectrometers from LWFA experiments with the DRACO laser at HZDR under influence of a mask in the laser beamline. ©2024 Team Electrons

6 Conclusion and Outlook

With the `FromOpenPMDPulse` profile, a valuable tool has been developed for the simulation software PIConGPU. It allows to simulate laser-plasma interaction using realistic laser profiles and addresses thus a long time weakness of PIC simulations. It opens up a path not only to recreate and validate experimental results, but also to investigate the influence of STCs and dispersion in realistic laser pulses, onto the properties of accelerated particles. With future parameter scans, e.g. over a range of GDD and TOD values or over the mask position and diameter, optimal parameter combinations can be revealed, e.g. for experimental LWFA setups, and optimized experimental designs can be proposed.

INSIGHT measurements can serve as realistic input data set for the `FromOpenPMD-Pulse` profile, because these provide the full field information about the laser pulse at the focus position. Such measurements have to undergo certain preparation steps before serving as simulation input, which have been described in chapter 3. The python script created for this purpose works independently from any PIConGPU simulations, which is why it additionally serves as tool to evaluate INSIGHT measurements.

Currently, INSIGHT measurements represent the most realistic laser model available for laser-plasma simulations. Nevertheless, there are a few limitations to this measurement principle. It is complex, time-consuming, and ultimately yields only an averaged result. The evolution of the phase with frequency is not measurable, leading to a loss of information regarding potential residual phases unless obtained through independent measurements. Additionally, the shot-to-shot fluctuations of the laser, observed experimentally, cannot be reproduced with INSIGHT. Unfortunately, these fluctuations complicate the measurement itself and can cause measurement artifacts. A limited frequency range poses challenges when converting the pulse to the time domain, and extending the frequency range increases the measurement duration. The limited spatial resolution of the camera may lead to a loss of information regarding the laser field distribution or necessitate the usage of alternative setups if the focal spot size is too small, e.g. for proton acceleration at HZDR. Consequently, INSIGHT measurements may exhibit slight discrepancies from the true laser field. Given the highly nonlinear nature of laser-plasma interactions in the relativistic regime, these discrepancies can lead to deviations between simulation results and experimental observations, as discussed in chapter 5 of this thesis.

A possible way forward to tackle the averaging issue is to reconstruct laser pulses from single-shot measurements, e.g. by applying a Hermite-Gauss mode decomposition and elements of the Gerchberg-Saxton algorithm to fluence measurements in the transverse plane at multiple positions along the propagation axis [45]. However, such

measurements have inherent limitations, including potential convergence issues, and have not yet been carried out at HZDR. Once these measurements become available, the `FromOpenPMDPulse` profile will be sufficiently versatile to incorporate these pulse profiles as input for simulations without any complications.

Until then, the `FromOpenPMDPulse` profile can be refactored according to the suggestions mentioned in chapter 4, to improve its accurateness and versatility, e.g. refactoring of the GPU memory allocation, enabling oblique propagation and oblique or circular polarisation together with the possibility of setting the transverse focal coordinates, and replacing the linear interpolation routine with a higher order.

Creating a digital twin of the experimental setup is one mayor goal of simulations. Not only a realistic laser profile is needed for this, but also a realistic plasma target. This presents a difficulty, as its true form and extent is unknown at the moment for LWFA experiments with the DRACO laser at HZDR. Hence, it can only be roughly estimated, leading to simplified setups. However, density fluctuations and variations in the extent of the plasma, which are most likely encountered in realistic plasma targets, influence electron injection and acceleration and should thus be included in realistic simulations.

In summary, the achievements and results of this thesis suggest three possible future pathways:

1. Improve the full experiment modelling by performing and including recent gas profile measurements,

2. Study the impact of intentionally tuned STCs in realistic laser pulses on laser-plasma acceleration,

3. Improve the laser modelling by developing a laser field reconstruction based on single-shot measurements.

Bibliography

[1] F. Kroll, F.-E. Brack, C. Bernert, S. Bock, E. Bodenstein, K. Brüchner, T. E. Cowan, L. Gaus, R. Gebhardt, U. Helbig, L. Karsch, T. Kluge, S. Kraft, M. Krause, E. Lessmann, U. Masood, S. Meister, J. Metzkes-Ng, A. Nossula, J. Pawelke, J. Pietzsch, T. Püschel, M. Reimold, M. Rehwald, C. Richter, H.-P. Schlenvoigt, U. Schramm, M. E. P. Umlandt, T. Ziegler, K. Zeil, and E. Beyreuther, "Tumour irradiation in mice with a laser-accelerated proton beam," Nature Physics **18**, 316 (2022).

[2] R. Betti and O. A. Hurricane, "Inertial-confinement fusion with lasers," Nature Physics **12**, 435 (2016).

[3] D. Kraus, J. Vorberger, A. Pak, N. J. Hartley, L. B. Fletcher, S. Frydrych, E. Galtier, E. J. Gamboa, D. O. Gericke, S. H. Glenzer, E. Granados, M. J. MacDonald, A. J. MacKinnon, E. E. McBride, I. Nam, P. Neumayer, M. Roth, A. M. Saunders, A. K. Schuster, P. Sun, T. van Driel, T. Döppner, and R. W. Falcone, "Formation of diamonds in laser-compressed hydrocarbons at planetary interior conditions," Nature Astronomy **1**, 606 (2017).

[4] C. Bernert, S. Assenbaum, F.-E. Brack, T. E. Cowan, C. B. Curry, M. Garten, L. Gaus, M. Gauthier, S. Göde, I. Goethel, S. H. Glenzer, T. Kluge, S. Kraft, F. Kroll, M. Kuntzsch, J. Metzkes-Ng, M. Loeser, L. Obst-Huebl, M. Rehwald, H.-P. Schlenvoigt, C. Schoenwaelder, U. Schramm, M. Siebold, F. Treffert, T. Ziegler, and K. Zeil, "Off-harmonic optical probing of high intensity laser plasma expansion dynamics in solid density hydrogen jets," Scientific Reports **12**, 7287 (2022).

[5] L. Yang, L. Huang, S. Assenbaum, T. E. Cowan, I. Goethel, S. Göde, T. Kluge, M. Rehwald, X. Pan, U. Schramm, J. Vorberger, K. Zeil, T. Ziegler, and C. Bernert, "Time-resolved optical shadowgraphy of solid hydrogen jets as a testbed to benchmark particle-in-cell simulations," Communications Physics **6**, 368 (2023).

[6] M. Labat et al., "Seeded free-electron laser driven by a compact laser plasma accelerator," Nature Photonics **17**, 150 (2023).

[7] T. Kluge, M. Rödel, J. Metzkes-Ng, A. Pelka, A. L. Garcia, I. Prencipe, M. Rehwald, M. Nakatsutsumi, E. E. McBride, T. Schönherr, M. Garten, N. J. Hartley, M. Zacharias, J. Grenzer, A. Erbe, Y. M. Georgiev, E. Galtier, I. Nam, H. J. Lee, S. Glenzer, M. Bussmann, C. Gutt, K. Zeil, C. Rödel, U. Hübner, U. Schramm, and T. E. Cowan, "Observation of Ultrafast Solid-Density Plasma

Dynamics Using Femtosecond X-Ray Pulses from a Free-Electron Laser," Phys. Rev. X **8**, 031068 (2018).

[8] N. P. Dover, T. Ziegler, S. Assenbaum, C. Bernert, S. Bock, F.-E. Brack, T. E. Cowan, E. J. Ditter, M. Garten, L. Gaus, I. Goethel, G. S. Hicks, H. Kiriyama, T. Kluge, J. K. Koga, A. Kon, K. Kondo, S. Kraft, F. Kroll, H. F. Lowe, J. Metzkes-Ng, T. Miyatake, Z. Najmudin, T. Püschel, M. Rehwald, M. Reimold, H. Sakaki, H.-P. Schlenvoigt, K. Shiokawa, M. E. P. Umlandt, U. Schramm, K. Zeil, and M. Nishiuchi, "Enhanced ion acceleration from transparency-driven foils demonstrated at two ultraintense laser facilities," Light: Science Applications **12**, 71 (2023).

[9] T. Ziegler, I. Göthel, S. Assenbaum, C. Bernert, F.-E. Brack, T. Cowan, N. P. Dover, L. Gaus, T. Kluge, S. Kraft, F. Kroll, J. Metzkes-Ng, M. Nishiuchi, I. Prencipe, T. Püschel, M. Rehwald, M. Reimold, H.-P. Schlenvoigt, M. E. P. Umlandt, M. A. V. Pinochet, U. Schramm, and K. Zeil, "Laser-driven high-energy proton beams from cascaded acceleration regimes," **20**, 1211 (2024).

[10] K. Birdsall and A. B. Langdon, *Plasma Physics via Computer Simulation (Series in Plasma Physics)*, 1st ed. (Taylor & Francis, New York, 2004).

[11] R. Pausch, M. Bussmann, J. P. Couperus Cabadağ, A. Irman, S. Schöbel, U. Schramm, K. Steiniger, R. Widera, and A. Debus, "Modeling Beyond Gaussian Laser Pulses in Particle-in-Cell Simulations - The Impact of Higher Order Laser Modes," in 2022 ieee advanced accelerator concepts workshop (aac) (2022), pp. 1–5.

[12] D. Strickland and G. Mourou, "Compression of amplified chirped optical pulses," Optics Communications **55**, 447 (1985).

[13] T. Ziegler, D. Albach, C. Bernert, S. Bock, F.-E. Brack, T. E. Cowan, N. P. Dover, M. Garten, L. Gaus, R. Gebhardt, I. Goethel, U. Helbig, A. Irman, H. Kiriyama, T. Kluge, A. Kon, S. Kraft, F. Kroll, M. Loeser, J. Metzkes-Ng, M. Nishiuchi, L. Obst-Huebl, T. Püschel, M. Rehwald, H.-P. Schlenvoigt, U. Schramm, and K. Zeil, "Proton beam quality enhancement by spectral phase control of a PW-class laser system," Scientific Reports **11**, 2045 (2021).

[14] A. Irman, J. P. Couperus, A. Debus, A. Köhler, J. M. Krämer, R. Pausch, O. Zarini, and U. Schramm, "Improved performance of laser wakefield acceleration by tailored self-truncated ionization injection," Plasma Physics and Controlled Fusion **60**, 044015 (2018).

[15] J. W. Goodman, *Introduction to Fourier Optics*, 3rd ed. (Roberts & Company Publishers, 2005).

[16] A. E. Siegman, *Lasers* (University Science Books, 1986).

[17] SourceLAB, *INSIGHT | Spatio-temporal metrology at focus of ultra-short laser pulses*, `https://www.sourcelab-plasma.com/laser-shaping/beam-shaping-catalog/insight/` (visited on 10/24/2024).

[18] K. Steiniger, F. Dietrich, D. Albach, M. Bussmann, A. Irman, M. Loeser, R. Pausch, T. Püschel, R. Sauerbrey, S. Schöbel, U. Schramm, M. Siebold, K. Zeil, and A. Debus, "Distortions in focusing laser pulses due to spatio-temporal couplings – An analytic description," High Power Laser Science and Engineering, 10.1017/hpl.2023.96 (2023).

[19] J.-C. Diels and W. Rudolph, *Ultrashort Laser Pulse Phenomena. Fundamentals, Techniques and Applications on a Femtosecond Time Scale*, 2nd ed. (Academic Press, 2006).

[20] A. Borot and F. Quéré, "Spatio-spectral metrology at focus of ultrashort lasers: a phase-retrieval approach," Opt. Express **26**, 26444 (2018).

[21] F. Dietrich, https://github.com/ComputationalRadiationPhysics/picongpu/blob/dev/lib/python/picongpu/extra/input/preparingInsightData.py (visited on 12/11/2024).

[22] NumPy Developers, *Discrete Fourier Transform (numpy.fft)*, https://numpy.org/doc/stable/reference/routines.fft.html (visited on 11/15/2024).

[23] G. Pariente, V. Gallet, A. Borot, O. Gobert, and F. Quéré, "Space–time characterization of ultra-intense femtosecond laser beams," Nature Photonics **10**, 547 (2016).

[24] The SciPy community, https://docs.scipy.org/doc/scipy/reference/generated/scipy.optimize.curve_fit.html (visited on 01/06/2025).

[25] The openPMD Community, *openPMD C++ Python API*, https://openpmd-api.readthedocs.io/en/0.15.2/index.html (visited on 10/29/2024).

[26] *PIConGPU - Particle-in-Cell Simulations for the Exascale Era*, https://github.com/ComputationalRadiationPhysics/picongpu (visited on 02/13/2025).

[27] K. Steiniger, *Hierarchy of Charge Assignment Schemes*, https://picongpu.readthedocs.io/en/latest/models/shapes.html (visited on 12/16/2024).

[28] A. Taflove and S. C. Hagness, *Computational Electrodynamics. The Finite Difference Time-Domain Method*, 3rd ed. (Artech House, Norwood, 2005).

[29] B. Ripperda, F. Bacchini, J. Teunissen, C. Xia, O. Porth, L. Sironi, G. Lapenta, and R. Keppens, "A Comprehensive Comparison of Relativistic Particle Integrators," The Astrophysical Journal Supplement Series **235**, 21 (2018).

[30] H. Qin, S. Zhang, J. Xiao, J. Liu, Y. Sun, and W. Tang, "Why is Boris algorithm so good?" Physics of Plasmas **20**, 10.1063/1.4818428 (2013).

[31] T. Esirkepov, "Exact charge conservation scheme for Particle-in-Cell simulation with an arbitrary form-factor," Computer Physics Communications **135**, 144 (2001).

[32] K. Steiniger, R. Widera, S. Bastrakov, M. Bussmann, S. Chandrasekaran, B. Hernandez, K. Holsapple, A. Huebl, G. Juckeland, J. Kelling, M. Leinhauser, R. Pausch, D. Rogers, U. Schramm, J. Young, and A. Debus, "EZ: An efficient, charge conserving current deposition algorithm for electromagnetic Particle-in-Cell simulations," Computer Physics Communications **291**, 108849 (2023).

[33] K. Steiniger, J. Trojok, and S. Bastrakov, *Finite-Difference Time-Domain Method*, `https://picongpu.readthedocs.io/en/latest/models/AOFDTD.html` (visited on 12/16/2024).

[34] H. Burau, R. Widera, W. Hönig, G. Juckeland, A. Debus, T. Kluge, U. Schramm, T. E. Cowan, R. Sauerbrey, and M. Bussmann, "PIConGPU: A Fully Relativistic Particle-in-Cell Code for a GPU Cluster," IEEE Transactions on Plasma Science **38**, 2831 (2010).

[35] E. Zenker, R. Widera, A. Huebl, G. Juckeland, A. Knüpfer, W. E. Nagel, and M. Bussmann, "Performance-Portable Many-Core Plasma Simulations: Porting PIConGPU to OpenPower and Beyond," in *High performance computing* (Springer International Publishing, 2016), pp. 293–301.

[36] K. Yee, "Numerical solution of initial boundary value problems involving Maxwell's equations in isotropic media," IEEE Transactions on Antennas and Propagation **14**, 302 (1966).

[37] S. Bastrakov, *Total Field/Scattered Field*, `https://picongpu.readthedocs.io/en/latest/models/total_field_scattered_field.html` (visited on 11/13/2024).

[38] M. Potter and J.-P. Bérenger, "A Review of the Total Field/Scattered Field Technique for the FDTD Method," FERMAT **19** (2017).

[39] T. Tajima and J. M. Dawson, "Laser Electron Accelerator," Phys. Rev. Lett. **43**, 267 (1979).

[40] E. Esarey, C. B. Schroeder, and W. P. Leemans, "Physics of laser-driven plasma-based electron accelerators," Rev. Mod. Phys. **81**, 1229 (2009).

[41] A. Pukhov and J. Meyer-ter-Vehn, "Laser wake field acceleration: the highly non-linear broken-wave regime," Applied Physics B **74**, 355 (2002).

[42] M. Zeng, M. Chen, Z.-M. Sheng, W. B. Mori, and J. Zhang, "Self-truncated ionization injection and consequent monoenergetic electron bunches in laser wakefield acceleration," Physics of Plasmas **21**, 030701 (2014).

[43] G.-Z. Sun, E. Ott, Y. C. Lee, and P. Guzdar, "Self-focusing of short intense pulses in plasmas," The Physics of Fluids **30**, 526 (1987).

[44] Y.-Y. Chang, J. C. Cabada ğ, A. Debus, A. Ghaith, M. LaBerge, R. Pausch, S. Schöbel, P. Ufer, U. Schramm, and A. Irman, "Reduction of the electron-beam divergence of laser wakefield accelerators by integrated plasma lenses," Phys. Rev. Appl. **20**, L061001 (2023).

[45] I. Moulanier, L. T. Dickson, F. Massimo, G. Maynard, and B. Cros, "Fast laser field reconstruction method based on a Gerchberg-Saxton algorithm with mode decomposition," J. Opt. Soc. Am. B **40**, 2450 (2023).

Acknowledgements

When I started working on this thesis almost a year ago, the dimension of the project seemed endless to me. Every problem I solved opened up three more, but step for step I worked myself through, which would have been impossible without the help and support of other people.

First of all, I want to express my gratitude to the directors of the institute of radiation physics at HZDR, Prof. Dr. Ulrich Schramm and Prof. Dr. Thomas Cowan, for being the reviewers of this thesis.

A special thanks goes out to my supervisor Dr. Klaus Steiniger for his continuous support. You were always there to answer my questions and never lost the confidence in my capabilities, no matter how stupid these questions were. You helped me finding the solutions to obstacles in my path and, in the end, liberating this work from inaccuracies and spelling mistakes (although I am sure I have missed a few). Without you, I would not have managed all that.

Although I would consider myself a theorist, this work is located at the boundary between theory and experiment. Therefore, I had the pleasure of working together with experimentalists of FWKT. Thanks to Thomas Püschel, I know how INSIGHT measurements work, without even having attended one in person. I also owe a thank you to the electron team, especially Dr. Arie Irman and Susanne Schöbel, who shared their knowledge about the effects of a mask in DRACO's beamline with me and provided the corresponding plots shown in this thesis.

I would also like to thank the CRP-Team at HZDR: thank you to René for providing answers to my programming questions and technical implementation difficulties, thank you to Jessica for lending me your plasma, thank you to Richard for helping me unravel the significations of my simulation results and optimize my setup, and thank you to Finn for being a walking PIConGPU documentation. I am grateful to have been able to work in such a great team.

Erklärung

Hiermit erkläre ich, dass ich die vorliegende Arbeit im Rahmen der Betreuung am Institut für Strahlenphysik ohne unzulässige Hilfe Dritter verfasst habe und alle verwendeten Quellen als solche gekennzeichnet habe.

Dresden, 16.01.2025 F. Dilich

Ort, Datum Unterschrift